

# Deep Ocean Temperatures through Time

Paul J Valdes<sup>1</sup>, Christopher R Scotese<sup>2</sup>, Daniel J Lunt<sup>1</sup>

<sup>1</sup> School of Geographical Sciences, University of Bristol, Bristol BS8 1SS, UK

<sup>2</sup> Northwestern University, Dept Earth & Planetary Sci, Evanston, IL USA

Correspondence to: Paul Valdes (P.J.Valdes@bristol.ac.uk)

## Abstract

Benthic oxygen isotope records are commonly used as a proxy for global mean surface temperatures during the late Cretaceous and Cenozoic, and the resulting estimates have been extensively used in characterising major trends and transitions in the climate system, and for analysing past climate sensitivity. However, some fundamental assumptions governing this proxy have rarely been tested. Two key assumptions are: (a) benthic foraminiferal temperatures are geographically well-mixed and are linked to surface high latitude temperatures, and (b) surface high latitude temperatures are well correlated with global mean temperatures. To investigate the robustness of these assumptions through geological time, we performed a series of 109 climate model simulations using a unique set of paleogeographical reconstructions covering the entire Phanerozoic at the stage-level. The simulations have been run for at least 5000 model years to ensure that the deep ocean is in dynamic equilibrium. We find that the correlation between deep ocean temperatures and global mean surface temperatures is good for the Cenozoic and thus the proxy data are reliable indicators for this time period, albeit with a standard error of 2K. This uncertainty has not normally been assessed and needs to be combined with other sources of uncertainty when, for instance, estimating climate sensitivity based on using  $\delta^{18}\text{O}$  measurements from benthic foraminifera. The correlation between deep and global mean surface temperature becomes weaker for pre-Cenozoic time periods (when the paleogeography is significantly different than the present-day). The reasons for the weaker correlation include variability in the source region of the deep water (varying hemispheres but also varying latitudes of sinking), the depth of ocean overturning (some extreme warm climates have relatively shallow and sluggish circulations weakening the link between surface and deep ocean), and the extent of polar amplification (e.g. ice albedo feedbacks). Deep ocean sediments prior to the Cretaceous are rare, so extending the benthic foram proxy further into deeper time is problematic, but the model results presented here would suggest that the deep ocean temperatures from such time periods would probably be an unreliable indicator of global mean surface conditions.

32

## 33 1. Introduction

34

35 One of the most widely used proxies for estimating global mean surface temperature through the  
36 last 100 million years is benthic  $\delta^{18}\text{O}$  measurements from deep sea foraminifera (Zachos et al.,  
37 2001), (Zachos et al., 2008), (Cramer et al., 2009), (Friedrich et al., 2012). Two key underlying  
38 assumptions are that  $\delta^{18}\text{O}$  from benthic foraminifera represents deep ocean temperature (with a  
39 correction for ice volume and any vital effects), and that the deep ocean water masses originate  
40 from surface water in polar regions. By further assuming that polar surface temperatures are well  
41 correlated with global mean surface temperatures, then deep ocean isotopes can be assumed to  
42 track global mean surface temperatures. More specifically, (Hansen et al., 2008), and (Hansen and  
43 Sato, 2012) argue that changes in high latitude sea surface temperatures are approximately  
44 proportional to global mean surface temperatures because changes are generally amplified at high  
45 latitudes but that this is offset because temperature change is amplified over land areas. They  
46 therefore directly equate changes in benthic ocean temperatures with global mean surface  
47 temperature.

48 The resulting estimates of global mean surface air temperature have been used to understand past  
49 climates (e.g. (Zachos et al., 2008)). Combined with estimates of atmospheric  $\text{CO}_2$  they have also  
50 been used to estimate climate sensitivity (e.g. (Hansen et al., 2013)) and hence contribute to the  
51 important ongoing debate about the likely magnitude of future climate change.

52 However, some of the underlying assumptions behind the method remains largely untested, even  
53 though we know that there are major changes to paleogeography and consequent changes in ocean  
54 circulation and location of deep-water formation in the deep past (e.g. (Lunt et al., 2010; Nunes and  
55 Norris, 2006); (Donnadieu et al., 2016); (Farnsworth et al., 2019a); (Ladant et al., 2020)). Moreover,  
56 the magnitude of polar amplification is likely to vary depending on the extent of polar ice caps, and  
57 changes in cloud cover (Sagoo et al., 2013), (Zhu et al., 2019). These issues are likely to modify the  
58 correlation between deep ocean temperatures and global mean surface temperature or, at the very  
59 least, increase the uncertainty in reconstructing past global mean surface temperatures.

60 The aim of this paper is two fold, (1) we wish to document the setup and initial results from a unique  
61 set of 109 climate model simulations of the whole Phanerozoic era (last 540 million years) at the  
62 stage level (approximately every 5 million years), and (2) we will use these simulations to investigate  
63 the accuracy of the deep ocean temperature proxy in representing global mean surface  
64 temperature.

65 The focus of the work is to examine the link between benthic ocean temperatures and surface  
66 conditions. However, we evaluate the fidelity of the model by comparing the model predicted ocean  
67 temperatures to estimates of the isotopic temperature of the deep ocean during the past 110  
68 million years ((Zachos et al., 2008), (Cramer et al., 2009), (Friedrich et al., 2012)), and model  
69 predicted surface temperatures to the sea surface temperatures estimates of (O'Brien et al., 2017)  
70 and (Cramwinckel et al., 2018). This gives us confidence that the model is behaving plausibly but we  
71 emphasise that the fidelity of the simulations is strongly influenced by the accuracy of CO<sub>2</sub> estimates  
72 through time. We then use the complete suite of climate simulations to examine changes in ocean  
73 circulation, ice formation, and the impact on ocean and surface temperature. Our paper will not  
74 consider any issues associated with assumptions regarding the relationship between deep-sea  
75 foraminifera  $\delta^{18}\text{O}$  and various temperature calibrations because our model does not simulate the  
76  $\delta^{18}\text{O}$  of sea water (or vital effects).

77

## 78 2. Simulation Methodology

### 79 2.1 Model Description

80 We use a variant of the Hadley Centre model, HadCM3 ((Pope et al., 2000), (Gordon et al., 2000))  
81 which is a coupled atmosphere-ocean-vegetation model. The specific version, HadCM3BL-M2.1aD, is  
82 described in detail in (Valdes et al., 2017). The model has a horizontal resolution of  $3.75^\circ \times 2.5^\circ$  in  
83 longitude/latitude (roughly corresponding to an average grid box size of  $\sim 300\text{km}$ ) in both the  
84 atmosphere and the ocean. The atmosphere has 19 unequally spaced vertical levels, and the ocean  
85 has 20 unequally spaced vertical levels. Though HadCM3 is relatively low resolution and low  
86 complexity model compared to the current CMIP5/CMIP6 state-of-the-art model, its performance at  
87 simulating modern climate is comparable to many CMIP5 models (Valdes et al., 2017). The  
88 performance of the dynamic vegetation model compared to modern observations is also described  
89 in (Valdes et al., 2017) but the modern deep ocean temperatures are not described in that paper.  
90 We therefore include a comparison to present day observed deep ocean temperatures in section  
91 3.1.

92 To perform paleo-simulations, several important modifications to the standard model described in  
93 (Valdes et al., 2017) must be incorporated:

- 94 (a) The standard pre-industrial model uses a prescribed climatological pre-industrial ozone  
95 concentration (i.e. prior to the development of the “ozone” hole) which is a function of  
96 latitude, atmospheric height, and month of the year. However, we do not know what the

97 distribution of ozone should be in these past climates. (Beerling et al., 2011) modelled small  
98 changes in tropospheric ozone for the early Eocene and Cretaceous but no comprehensive  
99 stratospheric estimates are available. Hence most paleoclimate model simulations assume  
100 unchanging concentrations. However, there is a problem with using a prescribed ozone  
101 distribution for paleo-simulations because it does not incorporate ozone feedbacks  
102 associated with changes in tropospheric height. During warm climates, the model predicts  
103 that the tropopause would rise. In the real world, ozone would track the tropopause rise,  
104 however, this rising ozone feedback is not included in our standard model. This leads to  
105 substantial extra warming and artificially increases the apparent climate sensitivity.  
106 Simulations of future climate change have shown that ozone feedbacks can lead to an over-  
107 estimate of climate sensitivity by up to 20% ((Dietmuller et al., 2014), (Nowack et al., 2015))  
108 (Hardiman et al., 2019). Therefore, to incorporate some aspects of this feedback, we have  
109 changed the ozone scheme in the model. Ozone is coupled to the model predicted  
110 tropopause height every model timestep in the following simple way:

- 111 •  $2.0 \times 10^{-8}$  kg/kg in the troposphere
- 112 •  $2.0 \times 10^{-7}$  kg/kg at the tropopause
- 113 •  $5.5 \times 10^{-6}$  kg/kg above the tropopause
- 114 •  $5.5 \times 10^{-6}$  kg/kg at the top model level.

115 These values are approximate averages of present-day values and were chosen so that the  
116 tropospheric climate of the resulting pre-industrial simulation was little altered compared  
117 with the standard preindustrial simulations; the resulting global mean surface air  
118 temperatures differed by only 0.05 °C. These modifications are similar to those used in the  
119 FAMOUS model (Smith et al., 2008) except that the values in the stratosphere are greater in  
120 our simulation, largely because our model vertical resolution is higher than in FAMOUS.

121 Note that these changes improve upon the scheme used by (Lunt et al., 2016) and  
122 (Farnsworth et al., 2019a). They used much lower values of stratospheric ozone and had no  
123 specified value at the top of the model. This resulted in their model having ~ 1°C cold bias  
124 for pre-industrial temperatures and may have also affected their estimates of climate  
125 sensitivity.

126 (b) The standard version of HadCM3 conserves the total volume of water throughout the  
127 atmosphere and ocean (including in the numerical scheme) but several processes in the  
128 model “lose or gain” water:

- 129           1. Snow accumulates over ice sheets but there is no interactive loss through iceberg  
130           calving resulting in an excess loss of fresh water from the ocean.
- 131           2. The model caps salinity at a maximum of 45 PSU (and a minimum of 0 PSU), by  
132           artificially adding/subtracting fresh water to the ocean. This mostly affects small  
133           enclosed seas (such as the Red Sea or enclosed Arctic) where the model does not  
134           represent the exchanges with other ocean basins.
- 135           3. Modelled river runoff includes some river basins which drain internally. These often  
136           correspond to relatively dry regions, but any internal drainage simply disappears  
137           from the model.
- 138           4. The land surface scheme includes evaporation from sub-grid scale lakes (which are  
139           prescribed as a lake fraction in each grid box, at the start of the run). The model  
140           does not represent the hydrological balance of these lakes, consequently the  
141           volume of the lakes does not change. This effectively means that there is a net  
142           source/sink of water in the model in these regions.

143           In the standard model, these water sources/sinks are approximately balanced by a flux of  
144           water into the surface ocean. This is prescribed at the start of the run and does not vary  
145           during the simulations. It is normally set to a pre-calculated estimate based on an old  
146           HadCM3-M1 simulation. The flux is strongest around Greenland and Antarctica and is  
147           chosen such that it approximately balances the water loss described in (1) i.e. the net snow  
148           accumulation over these ice sheets. There is an additional flux covering the rest of the  
149           surface ocean which approximately balances the water loss from the remaining three terms  
150           (2-4). The addition of this water flux keeps the global mean ocean salinity approximately  
151           constant on century time scales. However, depending on the simulation, the drift in average  
152           oceanic salinity can be as much as 1PSU per thousand years and thus can have a major  
153           impact on ultra-long runs of >5000 years (Farnsworth et al., 2019a).

154           For the paleo-simulations in this paper, we therefore take a slightly different approach.  
155           When ice sheets are present in the Cenozoic, we include the water flux (for the relevant  
156           hemisphere) described in (1) above, based on modern values of iceberg calving fluxes for  
157           each hemisphere. However, to ensure that salinity is conserved, we also interactively  
158           calculate an additional globally uniform surface water flux based on relaxing the volume  
159           mean ocean salinity to a prescribed value on a 20-year timescale. This ensures that there is  
160           no long-term trend in ocean salinity. Tests of this update on the pre-industrial simulations  
161           revealed no appreciable impact on the skill of the model relative to the observations. We

162 have not directly compared our simulations to the previous runs of the (Farnsworth et al.,  
163 2019a) because they use different CO<sub>2</sub> and different paleogeographies. However in practice,  
164 the increase of salinity in their simulations is well mixed and seems to have relatively little  
165 impact on the overall climate and ocean circulation.

166 We have little knowledge of whether ocean salinity has changed through time, and so keep  
167 the prescribed mean ocean salinity constant across all simulations.

168

## 169 2.2 Model Boundary Conditions

170 There are several boundary conditions that require modification through time. In this sequence of  
171 simulations, we only modify three key time-dependent boundary conditions: 1) the solar constant, 2)  
172 atmospheric CO<sub>2</sub> concentrations and, 3) paleogeographic reconstructions. We set the surface soil  
173 conditions to a uniform medium loam everywhere. All other boundary conditions (such as orbital  
174 parameters, volcanic aerosol concentrations etc.) are held constant at pre-industrial values.

175 The solar constant is based on (Gough, 1981) and increases linearly at an approximate rate of 11.1  
176 Wm<sup>-2</sup> per 100 Ma (0.8% per 100Ma), to 1365Wm<sup>-2</sup> currently. If we assume a planetary albedo of 0.3,  
177 and a climate sensitivity of 0.8 °C /Wm<sup>-2</sup> (approximately equivalent to 3°C per doubling of CO<sub>2</sub>), then  
178 this is equivalent to a temperature increase of ~.015°C per million years (~8°C over the whole of the  
179 Phanerozoic).

180 Estimates of atmospheric CO<sub>2</sub> concentrations have considerable uncertainty. We, therefore, use two  
181 alternative estimates (fig. 1a). The first uses the best fit Loess curve from (Foster et al., 2017), which  
182 is also very similar to the newer data from (Witkowski et al., 2018). The CO<sub>2</sub> levels have considerable  
183 short and long-term variability throughout the time period. Our second estimate removes much of  
184 the shorter term variability in the Foster (2017) curve. It was developed for two reasons. Firstly, a  
185 lot of the finer temporal structure in the Loess curve is a product of differing data density of the raw  
186 data and does not necessarily correspond to real features. Secondly, the smoother curve was heavily  
187 influenced by a previous (commercially confidential) sparser sequence of simulations using non-  
188 public paleogeographic reconstructions. The resulting simulations were generally in good agreement  
189 with terrestrial proxy datasets (Harris et al., 2017). Specifically, using commercial in confidence  
190 paleogeographies, we have performed multiple simulations at different CO<sub>2</sub> values for several stages  
191 across the last 440 million years and tested the resulting climate against commercial-in-confidence  
192 proxy data (Harris et al., 2017). We then selected the CO<sub>2</sub> that best matched the data. For the  
193 current simulations, we linearly interpolated these CO<sub>2</sub> values to every stage. The resulting CO<sub>2</sub>  
194 curve looks like a heavily smoothed version of the Foster curve and is within the (large) envelope of

195 CO<sub>2</sub> reconstructions. The first-order shapes of the two curves are similar, though they are very  
196 different for some time periods (e.g. Triassic and Jurassic). In practice, both curves should be  
197 considered an approximation to the actual evolution of CO<sub>2</sub> through time which remains uncertain.

198 We refer to the simulation using the second set of CO<sub>2</sub> reconstructions as the “smooth” CO<sub>2</sub>  
199 simulations, though it should be recognised that the Foster CO<sub>2</sub> curve has also been smoothed. The  
200 Foster CO<sub>2</sub> curve extends back to only 420 Ma, so we have proposed two alternative extensions back  
201 to 540 Ma. Both curves increase sharply so that the combined forcing of CO<sub>2</sub> and solar constant are  
202 approximately constant over this time period (Foster et al., 2017). The higher CO<sub>2</sub> in the Foster curve  
203 relative to the “smooth” curve is because the initial set of simulations showed that the Cambrian  
204 simulations were relatively cool compared to data estimates for the period (Henkes et al., 2018).

### 205 2.3 Paleogeographic Reconstructions

206 The 109 paleogeographic maps used in the HadleyCM3 simulations are digital representations of the  
207 maps in the PALEOMAP Paleogeographic Atlas (Scotese, 2016); (Scotese and Wright, 2018). Table 1  
208 lists all the time intervals that comprise the PALEOMAP Paleogeographic Atlas. The PaleoAtlas  
209 contains one map for nearly every stage in the Phanerozoic. A paleogeographic map is defined as a  
210 map that shows the ancient configuration of the ocean basins and continents, as well as important  
211 topographic and bathymetric features such as mountains, lowlands, shallow sea, continental  
212 shelves, and deep oceans. Paleogeographic reconstructions older than the oldest ocean floor (~Late-  
213 Jurassic) have uniform deep ocean floor depth.

214 Once the paleogeography for each time interval has been mapped, this information is then  
215 converted into a digital representation of the paleotopography and paleobathymetry. Each digital  
216 paleogeographic model is composed of over 6 million grid cells that capture digital elevation  
217 information at a 10 km x 10 km horizontal resolution and 40-meter vertical resolution. This  
218 quantitative, paleo-digital elevation model, or “paleoDEM”, allows us to visualize and analyse the  
219 changing surface of the Earth through time using GIS software and other computer modeling  
220 techniques. For use with the HadCM3L climate model, the original high-resolution elevation grid was  
221 reduced to a ~111 km x ~111 km (1° x 1°) grid.

222 For a detailed description of how the paleogeographic maps and paleoDEMs were produced the  
223 reader is referred to (Scotese, 2016); (Scotese and Schettino, 2017); (Scotese and Wright, 2018).  
224 (Scotese and Schettino, 2017) includes an annotated bibliography of the more than 100 key sources  
225 of paleogeographic information. Similar paleogeographic paleoDEMs have been produced by  
226 (Baatsen et al., 2016) and (Verard et al., 2015).

227 The raw paleogeographic data reconstructs paleo-elevations and paleo-bathymetry at a resolution of  
228  $1^\circ \times 1^\circ$ . These data were re-gridded to  $3.75^\circ \times 2.5^\circ$  resolution that matched the GCM using a simple  
229 area (for land sea mask) or volume (for orography and bathymetry) conserving algorithm. The  
230 bathymetry was lightly smoothed (using a binomial filter) to ensure that the ocean properties in the  
231 resulting model simulations were numerically stable. The high latitudes had this filter applied  
232 multiple times. The gridding sometimes produced single grid point enclosed ocean basins,  
233 particularly along complicated coastlines, and these were manually removed. Similarly, important  
234 ocean gateways were reviewed to ensure that the re-gridded coastlines preserved these structures.  
235 The resulting global fraction of land is summarized in fig.1b and examples are shown in figure 2. The  
236 original reconstructions can be found at [https://www.earthbyte.org/paleodem-resource-scotese-](https://www.earthbyte.org/paleodem-resource-scotese-and-wright-2018/)  
237 [and-wright-2018/](https://www.earthbyte.org/paleodem-resource-scotese-and-wright-2018/). Maps of each HadCM3L paleogeography are included in the supplementary  
238 figures.

239 The paleogeographic reconstructions also include an estimate of land ice area ((Scotese and Wright,  
240 2018); fig.1c). These were converted to GCM boundary conditions assuming a simple parabolic  
241 shape to estimate the ice sheet height. These ice reconstructions suggest small amounts of land ice  
242 were present during the early Cretaceous, unlike (Lunt et al., 2016) who used ice-free Cretaceous  
243 paleogeographies.

#### 244 2.4 Spin up Methodology

245 The oceans are the slowest evolving part of the modelled climate system and can take multiple  
246 millennia to reach equilibrium, depending on the initial condition and climate state. To speed up the  
247 convergence of the model, we initialized the ocean temperatures and salinity with the values from  
248 previous model simulations from similar time periods. The atmosphere variables were initialized in a  
249 similar manner.

250 Simulations were run in parallel so were not initialised from the previous stage results using these  
251 paleogeographies. In total, we performed almost 1 million years of model simulation and if we ran  
252 simulations in sequence, it would have taken 30 years to complete the simulations. By running these  
253 in parallel, initialised from previous modelling studies, we reduced the total run time to 3 months,  
254 albeit using a substantial amount of our high performance computer resources.

255 Although it is always possible that a different initialization procedure may produce different final  
256 states, it is impossible to explore the possibility of hysteresis/bistability without performing many  
257 simulations for each period, which is currently beyond our computing resources. Previous studies  
258 using HadCM3L (not published) with alternative ocean initial states (isothermal at 0C, 8C, and 16C)  
259 have not revealed multiple equilibria but this might have been because we did not locate the



260 appropriate part of parameter space that exhibits hysteresis. However, other studies have shown  
261 such behaviour (e.g. (Baatsen et al., 2018)). This remains a caveat of our current work and which we  
262 wish to investigate when we have sufficient computing resource.

263 The simulations were then run until they reached equilibrium, as defined by:

- 264 1. The globally and volume integrated annual mean ocean temperature trend is less than  
265  $1^{\circ}\text{C}/1000$  year, in most cases considerably smaller than this. We consider the volume  
266 integrated temperature because it includes all aspects of the ocean. However, it is  
267 dominated by the deep ocean trends and is near identical to the trends at a depth of 2731m  
268 (the lowest level that we have archived for the whole simulation).
- 269 2. The trends in surface air temperature are less than  $0.3^{\circ}\text{C}/1000$  year
- 270 3. The net energy balance at the top of the atmosphere, averaged over 100-year period at the  
271 end of the simulation, is less than  $0.25 \text{ Wm}^{-2}$  (in more than 80% of the simulations, the  
272 imbalance is less than  $0.1 \text{ Wm}^{-2}$ ). The Gregory plot (Gregory et al., 2004) implies surface  
273 temperatures are within  $0.3^{\circ}\text{C}$  of the equilibrium state.

274 These target trends chosen were somewhat arbitrary but are all less than typical orbital time scale  
275 variability (e.g. temperature changes since the last deglaciation were approximately  $5^{\circ}\text{C}$  over 10,000  
276 years). Most simulations were well within these criteria. 70% of simulations had residual net energy  
277 balances at the top of the atmosphere of less than  $0.1 \text{ Wm}^{-2}$ , but a few simulations were slower to  
278 reach full equilibrium. The strength of using multiple constraints is that a simulation may, by chance,  
279 pass one or two of these criteria but were unlikely to pass all three tests. For example, all the models  
280 that we extended failed at least two of the criteria. The resulting time series of volume integrated  
281 global, annual mean ocean temperatures are shown in fig. 3. The supplementary figures also include  
282 this for each simulation, as well as the trends at 2731m.

283 The “smooth”  $\text{CO}_2$  simulations were all run for 5050 model years and satisfied the criteria. The  
284 Foster- $\text{CO}_2$  simulations were initially run for a minimum of 2000 years (starting from the end of the  
285 5000 year runs), at which point we reviewed the simulations relative to the convergence criteria. If  
286 the simulations had not converged, we extended the runs for an additional 3000 years. If they had  
287 not converged at the end of 5000 years, we extended them again for an additional 3000 years. After  
288 8000 years, all simulations had converged based on the convergence criteria. In general, the slowest  
289 converging simulations corresponded to some of the warmest climates (final temperatures in figure  
290 3b and 3c were generally warmer than in figure 3a). It cannot be guaranteed that further changes  
291 will not occur; however, we note that the criteria and length of the simulations greatly exceed PMIP-  
292 LGM (Kageyama et al., 2017) and PMIP-DeepMIP (Lunt et al., 2017) protocols.



## 294 3. Results

### 295 3.1 Comparison of Deep Ocean Temperatures to Benthic Ocean Data

296 Before using the model to investigate the linkage of deep ocean temperatures to global mean  
297 surface temperatures, it is interesting to evaluate whether the modelled deep ocean temperatures  
298 agree with the deep ocean temperatures obtained from the isotopic studies of benthic foraminifera  
299 (Friedrich et al., 2012; Zachos et al., 2008). It is important to note that the temperatures are strongly  
300 influenced by the choice of CO<sub>2</sub>, so we are not expecting complete agreement, but we simply wish to  
301 evaluate whether the model is within plausible ranges. If the modelled temperatures were in  
302 complete disagreement with data, then it might suggest that the model was too far away from  
303 reality to allow us to adequately discuss deep ocean/surface ocean linkages. If the modelled  
304 temperatures are plausible, then it shows that we are operating within the correct climate space. A  
305 detailed comparison of modelled surface and benthic temperatures to data throughout the  
306 Phanerozoic, using multiple CO<sub>2</sub> scenarios, is the subject of a separate ongoing project.

307 Figure 4a compares the modelled deep ocean temperature to the foraminifera data from the  
308 Cenozoic and Cretaceous (115 Ma). The observed isotope data are converted to deep ocean  
309 temperature using the procedures described by (Hansen et al., 2013). The modelled deep  
310 temperature shown in fig.4a (solid line) is the average temperature at the bottom level of the model,  
311 excluding depths less than 1000m (to avoid continental shelf locations which are typically not  
312 included in benthic data compilations). The observed benthic data are collected from a range of  
313 depths and are rarely at the very deepest levels (e.g. the new cores in (Friedrich et al., 2011) range  
314 from current water depths ranging from 1899m to 3192m). Furthermore, large data compilations  
315 rarely include how the depth of a particular site changed with time, and thus effectively assume that  
316 any differences between basins and through time are entirely due to climate change and not to  
317 changes in depth. Hence throughout the rest of the paper we frequently use the modelled 2731m  
318 temperatures as a surrogate for the true benthic temperature. This is a pragmatic definition because  
319 the area of deep ocean reduces rapidly (e.g. there is typically only 50% of the globe deeper than  
320 3300m). To evaluate whether this procedure gave a reasonable result, we also calculated the global  
321 average temperature at the model level at a depth of 2731m. This is shown by the dashed line in  
322 figure 4a. In general, the agreement between model bottom water temperatures and 2731m  
323 temperatures is very good. The standard deviation between model bottom water and constant  
324 depth of 2731m is 0.7°C, and the maximum difference is 1.4°C. Compared to the overall variability,  
325 this is a relatively small difference and shows that it is reasonable to assume that the deep ocean has  
326 weak vertical gradients.

327 The total change in benthic temperatures over the late Cretaceous and Cenozoic is well reproduced  
328 by the model, with the temperatures associated with the “smooth” CO<sub>2</sub> record being particularly  
329 good. We do not expect the model to represent sub-stage changes (100,000’s of years) such as the  
330 PETM excursion or OAEs, but we do expect that the broader temperature patterns should be  
331 simulated.

332 Comparison of the two simulations illustrates how strongly CO<sub>2</sub> controls global mean temperature.  
333 The Foster-CO<sub>2</sub> driven simulation substantially differs from the estimates of deep-sea temperature  
334 obtained from benthic forams and is generally a poorer fit to data. The greatest mismatch between  
335 the Foster curve and the benthic temperature curve is during the late Cretaceous and early  
336 Paleogene. Both dips in the Foster-CO<sub>2</sub> simulations correspond to relatively low estimates of CO<sub>2</sub>  
337 concentrations. For these periods, the dominant source of CO<sub>2</sub> values for these periods is from  
338 paleosols (fig.1) and thus we are reliant on one proxy methodology. Unfortunately, the alternative  
339 CO<sub>2</sub> reconstructions of (Witkowski et al., 2018) have a data gap during this period.

340 A second big difference between the Foster curve and the benthic temperature curve occurs during  
341 the Cenomanian-Turonian. This difference is similarly driven by a low estimate of CO<sub>2</sub> in the Foster-  
342 CO<sub>2</sub> curve. These low CO<sub>2</sub> values are primarily based on stomatal density indices. As can be seen in  
343 figure 1, stomatal indices frequently suggest CO<sub>2</sub> levels lower than estimates obtained by other  
344 methods. The CO<sub>2</sub> estimates by (Witkowski et al., 2018) generally supports the higher levels of CO<sub>2</sub>  
345 (near to 1000 ppmv) that are suggested by the “smooth” CO<sub>2</sub> curve.

346 Both sets of simulations underestimate the warming during the middle Miocene. This issue has been  
347 seen before in other models e.g. (You et al., 2009), (Knorr et al., 2011), (Krapp and Jungclaus, 2011)  
348 (Goldner et al., 2014) (Steinhorsdottir, 2021). In order to simulate the surface warmth of the middle  
349 Miocene (15 Ma), CO<sub>2</sub> concentrations in the range 460–580 ppmv were required, whereas the CO<sub>2</sub>  
350 reconstructions for this period (Foster et al., 2017) are generally quite low (250-400ppmv). This  
351 problem may be either due to the climate models having too low a climate sensitivity or that the  
352 estimates of CO<sub>2</sub> are too low (Stoll et al., 2019).

353 The original compilation of (Zachos et al., 2008) represented a relatively small portion of the global  
354 ocean and the implicit assumption was made that these results represented the entire ocean basin.  
355 (Cramer et al., 2009) examined the data from an ocean basin perspective and suggested that these  
356 inter-basin differences were generally small during the Late Cretaceous and early Paleogene (90Ma –  
357 35 Ma) and the differences between ocean basins were larger during the late Paleogene and early  
358 Neogene. Our model largely also reproduces this pattern. Figure 5 shows the ocean temperature at  
359 2731 m during the late Cretaceous (69 Ma), the late Eocene (39 Ma) and the Oligocene (31 Ma) for

360 the “smooth”-CO<sub>2</sub> simulations. In the late Cretaceous, the model temperatures are almost identical  
361 in the North Atlantic and Pacific (8°C – 10°C). There is warmer deep water forming in the Indian  
362 Ocean (deep mixed layer depths, not shown), off the West coast of Australia (10°C – 12°C), but  
363 otherwise the pattern is very homogeneous. This is in agreement with some paleoreconstructions  
364 for the Cretaceous (e.g. (Murphy and Thomas, 2012)).

365 By the time we reach the late Eocene (39 Ma), the North Atlantic and Pacific remain very similar but  
366 cooler deep water (6°C – 8°C) is now originating in the South Atlantic. The South Atlantic cool  
367 bottom water source remains in the Oligocene, but we see a strong transition in the North Atlantic  
368 to an essentially modern circulation with the major source of deep, cold water occurring in the high  
369 southerly latitudes (3°C – 5°C) and strong gradient between the North Atlantic and Pacific.

370 Figure 5 also shows the modelled deep ocean temperatures for present day (Fig. 5d) compared to  
371 the World Ocean Atlas Data (fig. 5e). It can be seen that the broad patterns are well reproduced in  
372 the model, with good predictions of the mean temperature of the Pacific. The model is somewhat  
373 too warm in the Atlantic itself, and has a stronger plume from the Mediterranean than is shown in  
374 the observations.

375

### 376 3.2 Comparison of Model Sea Surface Temperature to Proxy Data

377 The previous section focused on benthic temperatures, but it is also important to evaluate whether  
378 the modelled sea surface temperatures are plausible (within the uncertainties of the CO<sub>2</sub>  
379 reconstructions). Figure 4b shows a comparison between the model simulations of sea surface  
380 temperature and two published synthesis of proxy SST data. (O'Brien et al., 2017) compiled TEX<sub>86</sub>  
381 and δ<sup>18</sup>O for the Cretaceous, separated into tropical and high-latitude (polewards of 48°) regions.  
382 (Cramwinckel et al., 2018) compiled early Cenozoic tropical SST data, using Tex<sub>86</sub>, δ<sup>18</sup>O, Mg/Ca and  
383 clumped isotopes. We compare these to modelled SST for the region 15°S to 15°N, and for the  
384 average of Northern and Southern hemispheres between 47.5° and 60°. The proxy data includes  
385 sites from all ocean basins and so we also examined the spatial variability within the model. This  
386 spatial variability consists of changes along longitude (effectively different ocean basins) and  
387 changes with latitude (related to the gradient between equator and pole). We therefore calculated  
388 the average standard deviation of SST relative to the zonal mean at each latitude (this is shown by  
389 the smaller tick marks) and the total standard deviation of SST relative to the regional average. In  
390 practice, the equatorial values are dominated by inter-basin variations and hence the two measures  
391 of spatial variability are almost identical. The high latitude variability has a bigger difference  
392 between the longitudinal variations and the total variability, because the equator-to-pole

393 temperature gradient (i.e. the temperatures at the latitude limits of the region are a few degrees  
394 warmer/colder than the average). The spatial variability was very similar for the “smooth”-CO<sub>2</sub> and  
395 Foster-CO<sub>2</sub> simulations so, for clarity, on figure 4b we only show the results as error bars on the  
396 model Foster-CO<sub>2</sub> simulations.

397 Overall, the comparison between model and data is generally reasonable. The modelled equatorial  
398 temperatures largely follow the data, albeit with considerable scatter in the data. Both simulations  
399 tend to be towards the warmest equatorial data in the early Cretaceous (Albian). These  
400 temperatures largely come from Tex<sub>86</sub> data. There are many  $\delta^{18}\text{O}$  based SST which are significantly  
401 colder during this period. This data almost exclusively comes from cores 1050/1052 which are in the  
402 Gulf of Mexico. It is possible that these data are offset due to a bias in the  $\delta^{18}\text{O}$  of sea water because  
403 of the relatively enclosed region. The Foster-CO<sub>2</sub> simulations are noticeably colder than the data at  
404 the Cenomanian peak warmth, which is presumably related to the relatively low CO<sub>2</sub> as discussed for  
405 the benthic temperatures. The benthic record also showed a cool (low CO<sub>2</sub>) bias in the late  
406 Cretaceous. This is not such an obvious feature of the surface temperatures. The Foster simulations  
407 are colder than the “smooth”-CO<sub>2</sub> simulations during the late Cretaceous but there is not a strong  
408 mismatch between model and data. Both simulations are close to the observations, though the  
409 “smooth”-CO<sub>2</sub> simulations better matches the high-latitude data (but is slightly poorer with the  
410 tropical data).

411 The biggest area of disagreement between model and data is at high latitudes in the mid-Cretaceous  
412 warm period. In common with previous work with this model in the context of the Eocene (Lunt et  
413 al., 2021) the model is considerably cooler than the data, with a 10-15°C mismatch between models  
414 and data. The polar sea surface temperature estimates may have a seasonal bias because  
415 productivity is likely to be higher during the warmer summer months and, if we select the summer  
416 season temperatures from the model, then the mismatch is slightly reduced by about 4°C. The  
417 problem of a cool high latitudes in models is seen in many model studies and there is increasing  
418 evidence that this is related to the way that the models simulate clouds ((Kiehl and Shields, 2013);  
419 (Sagoo et al., 2013); (Upchurch et al., 2015; Zhu et al., 2019)). Of course, in practice deep water is  
420 formed during winter so the benthic temperatures do not suffer from a summer bias.

### 421 3.3 Correlation of Deep Ocean Temperatures to Polar Sea Surface Temperatures

422 The previous sections showed that that the climate model was producing a plausible reconstruction  
423 of past ocean temperature changes, at least within the uncertainties of the CO<sub>2</sub> estimates. We now  
424 use the HadCM3L model to investigate the links between deep ocean temperature and global mean  
425 surface temperature.

426 In theory, the deep ocean temperature should be correlated with the sea surface temperature at the  
427 location of deep-water formation which is normally assumed to be high latitude surface waters in  
428 winter. We therefore compare deep ocean temperatures (defined as the average temperature at the  
429 bottom of the model ocean, where the bottom must be deeper than 1000 m) with the average  
430 winter sea surface temperature polewards of 60° (fig. 6). Winter is defined as December, January,  
431 and February in the northern hemisphere and June, July, and August in the southern hemisphere.  
432 Also shown in Figure 6 is the best fit line, which has a slope of 0.40 (+/-0.05 at the 97.5% level), an  $r^2$   
433 of 0.59, and a standard error of 1.2°C. We obtained very similar results when we compared the polar  
434 sea surface temperatures with the average temperature at 2116m instead of the true benthic  
435 temperatures. We also compared the deep ocean temperatures to the mean polar sea surface  
436 temperatures when the mixed layer depth exceeded 250 m (poleward of 50°). The results were  
437 similar although the scatter was somewhat larger ( $r^2=0.48$ ).

438 Overall, the relationship between deep ocean temperatures and polar sea surface temperatures is  
439 clear (Figure 6) but there is considerable scatter around the best fit line, especially at the high end,  
440 and the slope is less steep than perhaps would be expected (Hansen and Sato, 2012). The scatter is  
441 less for the Cenozoic and late Cretaceous (up to 100 Ma; green and orange dots and triangles). If we  
442 used only Cenozoic and late Cretaceous simulations, then the slope is similar (0.43) but  $r^2=0.92$  and  
443 standard error=0.47°C. This provides strong confirmation that benthic data is a robust  
444 approximation to polar surface temperatures when the continental configuration is similar to the  
445 present.

446 However, the scatter is greater for older time periods, with the largest divergence observed for the  
447 warm periods of the Triassic and early Jurassic, particularly for the Foster CO<sub>2</sub> simulations (purple  
448 and blue dots). Examination of climate models for these time periods reveals relatively sluggish and  
449 shallow ocean circulation, with weak horizontal temperature gradients at depth (though salinity  
450 gradients can still be important, (Zhou et al., 2008)). For instance, in the Ladinian stage, mid-Triassic  
451 (~240Ma) the overturning circulation is extremely weak (Fig. 7). The maximum strength of the  
452 northern hemisphere overturning cell is less than 10 Sv and the southern cell is less than 5 Sv. Under  
453 these conditions, deep ocean water does not always form at polar latitudes. Examination of the  
454 mixed layer depth (not shown) shows that during these time periods, the deepest mixed layer  
455 depths are in the sub-tropics. In subtropics, there is very high evaporation relative to precipitation  
456 (due to the low precipitation and high temperature. This produces highly saline waters that sink and  
457 spread out into the global ocean.

458 This mechanism has been previously suggested as a mechanism for warm Cretaceous deep water  
459 formation (Brass et al., 1982), (Kennett and Stott, 1991). The idea that deep water may form in the

460 tropics is in disagreement with early hypothesis (e.g. (Emiliani, 1954)) but they were only considering  
461 the Tertiary and our model does not simulate any low latitude deep water formation during this  
462 period. We only see significant tropical deep water formation for earlier periods, and this has  
463 previously been suggested as a mechanism for warm Cretaceous deep water formation (Brass et al.,  
464 1982). Deep water typically forms in convective plumes. They showed that the depth and spreading  
465 of these plumes is related to the buoyancy flux with the greatest flux leading to bottom water and  
466 plumes of lesser flux leading to intermediate water. (Brass et al., 1982) suggested that this could  
467 occur in warm conditions in the tropics, particularly if there was significant epicontinental seaways  
468 and hypothesised that it “has been a dominant mechanism of deep water formation in historical  
469 times”. It is caused by a strong buoyancy flux linked to strong evaporation at high temperatures.

470

471 Our computer model simulations are partly consistent with this hypothesis. The key aspect for the  
472 model is a relatively enclosed seaway in the tropics and warm conditions. The paleogeographic  
473 reconstructions (see supplementary figures) suggest an enclosed Tethyan-like seaway starting in the  
474 Carboniferous and extending through to the Jurassic and early Cretaceous. However, the colder  
475 conditions of the Carboniferous prevents strong tropical buoyancy fluxes. However, when we get  
476 into the Triassic and Jurassic, the warmer conditions lead to strong evaporation at low latitudes and  
477 bottom water formation in the tropics. This also explains why we see more tropical deep water (and  
478 hence poorer correlations between deep and polar surface temperatures in figure 6) when using the  
479 Foster CO<sub>2</sub> since this is generally higher (and hence warmer) than the smoothed record.

480

481 An example of the formation of tropical deep water is shown in fig. 8. This shows a vertical cross-  
482 section of temperature and salinity near the equator for the Ladinian stage, mid-Triassic (240Ma).  
483 The salinity and temperature cross-section clearly shows high salinity warm waters sinking to the  
484 bottom of the ocean and spreading out. This is further confirmed by the water age tracer, fig. 9. This  
485 shows the water age (measured as time since it experienced surface conditions, see (England, 1995))  
486 at 2731m in the model for the Permian, Triassic, Cretaceous and present day. The present day  
487 simulation shows that the youngest water is in the N. Atlantic and off the coast of Antarctica,  
488 indicating that this is where the deep water is forming. By contrast, the Triassic period shows that  
489 the youngest water is in the tropical Tethyan region and that it spreads out from there to fill the rest  
490 of the ocean basin. There is no young water at high latitudes, confirming that the source of bottom  
491 water is tropical only. For the Permian, although there continues to be a Tethyan-like tropical  
492 seaway, the colder conditions mean that deep water is again forming at high latitudes only. The



493 Cretaceous is more complicated. It shows younger water in the high latitudes, but also shows some  
494 young water in the Tethys which merges with the high latitude waters. Additional indicator of the  
495 transitional nature of the Cretaceous are the mixed layer depth (see supplementary figures). This is  
496 a measure of where water is mixing to deeper levels. For this time period, there are regions of deep  
497 mixed layer in both the tropics and high latitudes, whereas it is only deep in the tropics for the  
498 Triassic and at high latitudes for present day.

499

500 This mechanism for warm deep water formation has also been seen in other climate models (e.g.  
501 (Barron and Peterson, 1990)). However, (Poulsen et al., 2001) conclude that in his model of the  
502 Cretaceous high-latitudes sources of deep water diminish with elevated CO<sub>2</sub> concentrations but did  
503 not see the dominance of tropical sources. Other models (e.g. (Ladant et al., 2020)) do not show any  
504 significant tropical deep water formation, suggesting that this feature is potentially a model-  
505 dependent result.

506 The correlation between deep ocean temperatures and the temperature of polar surface waters  
507 differs between the “smooth” CO<sub>2</sub> simulations and the Foster CO<sub>2</sub> simulations. The slope is only 0.30  
508 ( $r^2=0.57$ ) for the “smooth” CO<sub>2</sub> simulations whereas the slope is 0.48 ( $r^2=0.65$ ) for the Foster  
509 simulations. This is because CO<sub>2</sub> is a strong forcing agent that influences both the surface and deep  
510 ocean temperatures. By contrast, if the CO<sub>2</sub> does not vary as much, then the temperature does not  
511 vary as much, and the influence of paleogeography becomes more important. These  
512 paleogeographic changes generally cause subtle and complicated changes in ocean circulation that  
513 affect the location and latitude of deep-water formation.

514 In contrast, the mid-Cretaceous is also very warm but the continental configuration (specifically, land  
515 at high southern latitudes) favours the formation of cool, high latitude deep water. Throughout the  
516 Cretaceous there is significant southern high latitude source of deep water and hence deep-water  
517 temperatures are well correlated with surface high latitude temperatures. The strength of this  
518 connection, however, may be over exaggerated in the model. Like many climate models, HadCM3  
519 underestimates the reduction in the pole-to-Equator sea surface temperature (Lunt et al., 2012),  
520 (Lunt et al., 2021). This means that during the Cretaceous the high latitudes are probably too cold.  
521 Consequently, some seasonal sea ice does form which encourages the formation of cold deep-water,  
522 via brine rejection.

523 In the late Eocene (~40 Ma), the ocean circulation is similar to the Cretaceous, but the strong  
524 southern overturning cell is closer to the South Pole, indicating that the main source of deep water  
525 has moved further polewards. The poleward movement of the region of downwelling waters

526 explains some of the variability between deep ocean temperatures and temperature of polar surface  
527 waters.

528 For reference, we also include the present-day meridional circulation. The modern southern  
529 hemisphere circulation is essentially a strengthening of late Eocene meridional circulation. The  
530 Northern hemisphere is dominated by the Atlantic meridional overturning circulation. The Atlantic  
531 circulation pattern does not resemble the modern pattern of circulation until the Miocene.

### 532 3.4 Surface Polar Amplification

533

534 The conceptual model used to connect benthic ocean temperatures to global mean surface  
535 temperatures assumes that there is a constant relationship between high latitude sea surface  
536 temperatures and global mean annual mean surface air temperature. (Hansen and Sato, 2012)  
537 argue that this amplification is partly related to ice-albedo feedback but also includes a factor  
538 related to the contrasting amplification of temperatures on land compared to the ocean. To  
539 investigate the stability of this relationship, fig. 10 shows the correlation between polar winter sea  
540 surface temperatures ( $60^{\circ}$  -  $90^{\circ}$ ) and global mean surface air temperature. The polar temperatures  
541 are the average of the two winter hemispheres (i.e. average of DJF polar SSTs in the Northern  
542 hemisphere and JJA polar SSTs in the Southern hemisphere). Also shown is a simple linear  
543 regression, with an average slope of 1.3 and with an  $r^2 = 0.79$ . If we only use Northern polar winter  
544 temperatures, the slope is 1.1; if we only use Southern polar winter temperatures, then the slope is  
545 0.7. Taken separately, the scatter about the mean is considerably larger ( $r^2$  of 0.5 and 0.6  
546 respectively) than the scatter if both data sets are combined ( $r^2 = 0.79$ ). The difference between the  
547 southern and northern hemisphere response complicates the interpretation of the proxies and leads  
548 to potentially substantial uncertainties.

549 As expected, there appears to be a strong non-linear component to the correlation. There are two  
550 separate regimes: 1) one with a steeper slope during colder periods (average polar winter  
551 temperature less than about  $1^{\circ}\text{C}$ ), and 2) a shallower slope for warmer conditions. This is strongly  
552 linked to the extent of sea-ice cover. Cooler periods promote the growth of sea-ice which  
553 strengthens the ice-albedo feedback mechanism resulting in a steeper overall temperature gradient  
554 (strong polar amplification). Of course, the ocean sea surface temperatures are constrained to be -  
555  $2^{\circ}\text{C}$  but an expansion of seaice moves this further equatorward. Conversely, the warmer conditions  
556 result in less sea ice and hence a weaker sea ice-albedo feedback resulting in a weaker temperature  
557 gradient (reduced polar amplification).

558 Examining the Foster CO<sub>2</sub> and “smooth” CO<sub>2</sub> simulations reveals an additional factor. If we examine  
559 the “smooth” CO<sub>2</sub> simulations only, then the best fit linear slope is slightly less than the average  
560 slope (1.1 vs 1.3). This can be explained by the fact that we have fewer very cold climates  
561 (particularly in the Carboniferous) due to the relatively elevated levels of CO<sub>2</sub>. However, the scatter  
562 in the “smooth” CO<sub>2</sub> correlation is much larger, with an  $r^2$  of only 0.66. By comparison, correlation  
563 between Global Mean Surface Temperature and Polar Sea Surface Temperature using the Foster CO<sub>2</sub>  
564 has a similar overall slope to the combined set and a smaller amount of scatter. This suggests that  
565 CO<sub>2</sub> forcing and polar amplitude forcing have an important impact on the relationship between  
566 global and polar temperatures. The variations of carbon dioxide in the Foster set of simulations are  
567 large and they drive large changes in global mean temperature. Conversely significant sea-ice albedo  
568 feedbacks characterize times when the polar amplification is important. There are several well  
569 studied processes that lead to such changes, including albedo effects from changing ice but also  
570 from poleward heat transport changes, cloud cover, and latent heat effects ((Alexeev et al., 2005;  
571 Holland and Bitz, 2003; Sutton et al., 2007)). By contrast, the “smooth” CO<sub>2</sub> simulations have  
572 considerably less forcing due to CO<sub>2</sub> variability which leads to a larger paleogeographic effect. For  
573 instance, when there is more land at the poles, there will be more evaporation over the land areas  
574 and hence simple surface energy balance arguments would suggest different temperatures ((Sutton  
575 et al., 2007)) .

576 In figure 10, there are a few data points which are complete outliers. These correspond to  
577 simulations in the Ordovician; the outliers happen irrespective of the CO<sub>2</sub> model that is used.  
578 Inspection of these simulations shows that the cause for this discrepancy is related to two factors:  
579 1) a continental configuration with almost no land in the Northern hemisphere and , 2) a  
580 reconstruction which includes significant southern hemisphere ice cover (see fig.1 and fig 2).  
581 Combined, these factors produced a temperature structure which is highly non-symmetric, with the  
582 Southern high latitudes being more than 20°C colder than the Northern high latitudes. This anomaly  
583 biases the average polar temperatures shown in figure 10.

### 584 3.5 Deep Ocean Temperature versus Global Mean Temperature 585

586 The relationships described above help to understand the overall relationship between deep ocean  
587 temperatures and global mean temperature. Figure 11 shows the correlation between modelled  
588 deep ocean temperatures (> 1000 m) and global mean surface air temperature, and figure 12 shows  
589 a comparison of changes in modelled deep ocean temperature compared to model global mean  
590 temperature throughout the Phanerozoic.

591 The overall slope is 0.64 (0.59 to 0.69) with an  $r^2 = 0.74$ . If we consider the last 115 Ma (for which  
592 exists compiled benthic temperatures), then the slope is slightly steeper (0.67 with an  $r^2 = 0.90$ ).  
593 Similarly, the “smooth”-CO<sub>2</sub> and the Foster-CO<sub>2</sub> simulation results have very different slopes. The  
594 “smooth”-CO<sub>2</sub> simulations have a slope of 0.47, whereas the Foster-CO<sub>2</sub> simulations have a slope of  
595 0.76. The root mean square departure from the regression line in figure 11 is 1.3°C. Although we  
596 could have used a non-linear fit as we might expect such a relationship if the pole-to-equator  
597 temperature gradient changes, all use of benthic temperatures as a global mean surface  
598 temperature proxy are based on linear relationship.

599

600 The relatively good correlations in the fig.11 are confirmed when examining fig.12a and 12b. On  
601 average, the deep ocean temperatures tend to underestimate the global mean change (fig.12b)  
602 which is consistent with the regression slope being less than 1. However, the errors are substantial  
603 with largest errors occurring during the pre-Cretaceous and can be 4-6 °C. This is an appreciable  
604 error that would have a substantial impact on estimates of climate sensitivity. Even within the late  
605 Cretaceous and Cenozoic, the errors can exceed 2°C which can exceed 40% of the total change.

606 The characteristics of the plots can best be understood in terms of figures (6 and 10). For instance,  
607 most of the Carboniferous simulations plot below the regression line because the polar SSTs are not  
608 well-correlated with the global mean temperature (figure 10). By contrast, the Triassic and Jurassic  
609 Foster CO<sub>2</sub> simulations plot above the regression line because the deep ocean temperature is not  
610 well-correlated with the polar temperatures (figure 6).

#### 611 4. Discussion and Conclusion

612 The paper has presented the results from two unique sets of paleoclimate simulations covering the  
613 Phanerozoic. The focus of the paper has been to use the HadCM3L climate model to evaluate how  
614 well we can predict global mean surface temperatures from benthic foram data. This is an important  
615 consideration because benthic microfossil data are one of the few datasets used to directly estimate  
616 past global mean temperatures. Other methods, such as using planktonic foraminiferal estimates,  
617 are more challenging because the sample sites are geographically sparse, so it is difficult to  
618 accurately estimate the global mean temperature from highly variable and widely dispersed data.  
619 This is particularly an issue for older time periods when fewer isotopic measurements from  
620 planktonic microfossils are available, and can result in a bias because most of the isotopic  
621 temperature sample localities are from tropical latitudes (30°S – 30°N) (Song et al., 2019).

622 By contrast, deep ocean temperatures are more spatially uniform. Hence. benthic foram data has  
623 frequently been used to estimate past global mean temperatures and climate sensitivity (Hansen et

624 al., 2013). Estimates of uncertainty for deep ocean temperatures incorporate uncertainties from CO<sub>2</sub>  
625 and from the conversion of  $\delta^{18}\text{O}$  measurements to temperature but have not been able to assess  
626 assumptions about the source regions for deep ocean waters and the importance polar  
627 amplification. Of course, in practice, lack of ocean sea floor means that benthic compilations exist  
628 only for the last 110Ma.

629 Changes in heat transport also play a potentially important role in polar amplification. In the  
630 supplementary figure, we show the change in atmosphere and ocean poleward heat fluxes for each  
631 time period. Examination of the modelled poleward heat transport by the atmosphere and ocean  
632 shows a very complicated pattern, with all time periods showing the presence of some Bjerknes  
633 compensation (Bjerknes, 1964) (see (Outten et al., 2018) for example in CMIP5 models). Bjerknes  
634 compensation is where the change in ocean transport is largely balanced by an equal but opposite  
635 change in atmospheric transport. For instance, compared to present day, the mid-Cretaceous and  
636 Early Eocene warm simulations shows a large increase in northward atmospheric heat transport,  
637 linked with enhanced latent heat transport associated with the warmer, moister atmosphere.  
638 However, this is partly cancelled by an equal but opposite change in the ocean transport. E.g.  
639 compared to present day, the early Eocene northern hemisphere atmospheric heat transport  
640 increases by up to 0.5PW, but the ocean transport is reduced by an equal amount. The net  
641 transport from equator to the N.Pole changes by less than 0.1PW (i.e. less than 2% of total). Further  
642 back in time, the compensation is still apparent but the changes are more complicated, especially  
643 when the continents are largely in the Southern hemisphere. Understanding the causes of these  
644 transport changes will be the subject of another paper.

645 We have shown that although the expected correlation between benthic temperatures and high-  
646 latitude surface temperatures exists, the correlation has considerable scatter. This is caused by  
647 several factors. Changing paleogeographies results in changing locations for deep water formation.  
648 Some paleogeographies result in significant deep-water formation in the Northern hemisphere (e.g.  
649 our present-day configuration) although for most of the Phanerozoic, the dominant source of deep-  
650 water formation has been southern hemisphere. Similarly, even when deep water is formed in just  
651 one hemisphere, there can be substantial regional and latitudinal variations in its location and the  
652 corresponding temperatures. Finally, during times of very warm climates (e.g. mid-Cretaceous) the  
653 overturning circulation can be very weak and there is a marked decoupling between the surface  
654 waters and deep ocean. In the HadCM3 model during hothouse time periods, high temperatures and  
655 high rates of evaporation produce hot and saline surface waters which sink to become intermediate  
656 and deep waters at low latitudes.

657 Similar arguments can be made regarding the link between global mean temperature and the  
658 temperature at high latitudes. Particularly important is the area of land at the poles and the extent  
659 of sea ice/land ice. Colder climates and paleogeographic configurations with more land at the pole  
660 will result in a steeper latitudinal temperature gradient and hence exhibit a changing relationship  
661 between polar and global temperatures. But the fraction of land versus ocean is also important.

662 Finally, the overall relationship between deep ocean temperatures and global mean temperature is  
663 shown to be relatively linear, but the slope is quite variable. In the model simulations using the  
664 “smooth” CO<sub>2</sub> curve, the slope is substantially shallower (0.48) than slope obtained using the Foster  
665 CO<sub>2</sub> curve (0.76). This is related to the different controls that CO<sub>2</sub> and paleogeography exert (as  
666 discussed above). In the simulation that uses the “smooth” CO<sub>2</sub> data set, the levels of CO<sub>2</sub> do not  
667 vary much, so the paleogeographic controls are more pronounced.

668 This raises the interesting conundrum that when trying to use reconstructed deep ocean  
669 temperatures and CO<sub>2</sub> to estimate climate sensitivity, the interpreted global mean temperature also  
670 depends, in part, on the CO<sub>2</sub> concentrations. However, if we simply use the combined slope, then  
671 the root mean square error is approximately 1.4°C, and the maximum error is over 4°C. The root  
672 mean square error is a relatively small compared to the overall changes and hence the resulting  
673 uncertainty in climate sensitivity associated with this error is relatively small (~15%) and the CO<sub>2</sub>  
674 uncertainty dominates. However, the maximum error is potentially more significant.

675 Our work has not addressed other sources of uncertainty. In particular, it would be valuable to use a  
676 water isotope-enabled climate model to better address the uncertainties associated with the  
677 conversion of the observed benthic δ<sup>18</sup>O to temperature. This requires assumptions about the δ<sup>18</sup>O  
678 of sea water. We hope to perform such simulation in future work, though this is a particularly  
679 challenging computational problem because the isotope enabled model is significantly slower and  
680 the completion of the multi-millennial simulations required for deep ocean estimates would take  
681 more than 18 months to complete.

682 Our simulations extend and develop those published by (Lunt et al., 2016), and (Farnsworth et al.,  
683 2019a; Farnsworth et al., 2019b). The simulations reported in this paper used the same climate  
684 model (HadCM3L) but used an improved ozone concentration and corrected a salinity drift that can  
685 lead to substantial changes over the duration of the simulation. Our simulations also use an  
686 alternative set of geographic reconstructions that cover a larger time period (540 Ma – Modern).  
687 They also include realistic land ice cover estimates, which were not included in the original  
688 simulations (except for the late Cenozoic) but generally have a small impact in the Mesozoic.

689 Similarly, the new simulations use two alternative models for past atmospheric CO<sub>2</sub> use more  
690 realistic variations in CO<sub>2</sub> through time (compared with idealised constant values in Farnsworth et al  
691 and Lunt et al), while at the same time recognizing the levels of uncertainty. Although the Foster CO<sub>2</sub>  
692 curve is more directly constrained by CO<sub>2</sub> data, it should be noted that this data come from multiple  
693 proxies and there are large gaps in the data set. There is evidence that the different proxies have  
694 different biases and it is not obvious that the correct approach is to simply fit a Loess-type curve to  
695 the CO<sub>2</sub> data. This is exemplified by the Maastrichtian. The Foster Loess curve shows a minimum in  
696 CO<sub>2</sub> during the Maastrichtian which results in the modelled deep ocean temperatures being much  
697 too cold. However, detailed examination of the CO<sub>2</sub> data shows most of the Maastrichtian data is  
698 based on stomatal index reconstructions which often are lower than other proxies. Thus, the  
699 Maastrichtian low CO<sub>2</sub>, relative to other periods, is potentially driven by changing the proxy rather  
700 than by real temporal changes.

701 Though the alternative, “smooth” CO<sub>2</sub> curve is not the optimum fit to the data, it does pass through  
702 the cloud of individual CO<sub>2</sub> reconstructions and hence represents one possible “reality”. For the Late  
703 Cretaceous and Cenozoic, the “smooth” CO<sub>2</sub> simulation set does a significantly better job simulating  
704 the deep ocean temperatures of the Friedrich/Cramer/Zachos curve.

705 Although the focus of the paper has been the evaluation of the modelled relationship between  
706 benthic and surface temperatures, the simulations are a potentially valuable resource for future  
707 studies. This includes using the simulations for paleoclimate/climate dynamic studies and for climate  
708 impact studies, such as ecological niche modelling. We have therefore made available on our  
709 website the results from our simulations

710 ([https://www.paleo.bristol.ac.uk/ummodel/scripts/papers/Valdes\\_et\\_al\\_2021.html](https://www.paleo.bristol.ac.uk/ummodel/scripts/papers/Valdes_et_al_2021.html))

711 Data Availability

712 All simulation data is available from:

713 [https://www.paleo.bristol.ac.uk/ummodel/scripts/papers/Valdes\\_et\\_al\\_2021.html](https://www.paleo.bristol.ac.uk/ummodel/scripts/papers/Valdes_et_al_2021.html)

714 Author contributions

715 Study was developed by all authors. All model simulations were performed by PJV who also  
716 prepared the manuscript with contributions from all co-authors.

717 Competing interests

718 The authors declare that they have no conflict of interest

719

720

721 Acknowledgments.

722 DJL and PJV acknowledge funding from NERC through NE/P013805/1. The production of  
723 paleogeographic digital elevation models was funded by the sponsors of the PALEOMAP Project.  
724 This work is part of the PhanTASTIC project led by Scott Wing and Brian Huber from the Smithsonian  
725 Institution's National Museum of Natural History and was initiated at a workshop supported by  
726 Roland and Debra Sauermann. This work was carried out using the computational facilities of the  
727 Advanced Computing Research Centre, University of Bristol (<http://www.bris.ac.uk/acrc/>). The  
728 authors declare that they have no competing interests. Data and materials availability: All data  
729 needed to evaluate the conclusions in the paper are present in the paper. Model data can be  
730 accessed at [www.bridge.bris.ac.uk/resources/simulations](http://www.bridge.bris.ac.uk/resources/simulations).

731

732

733

734

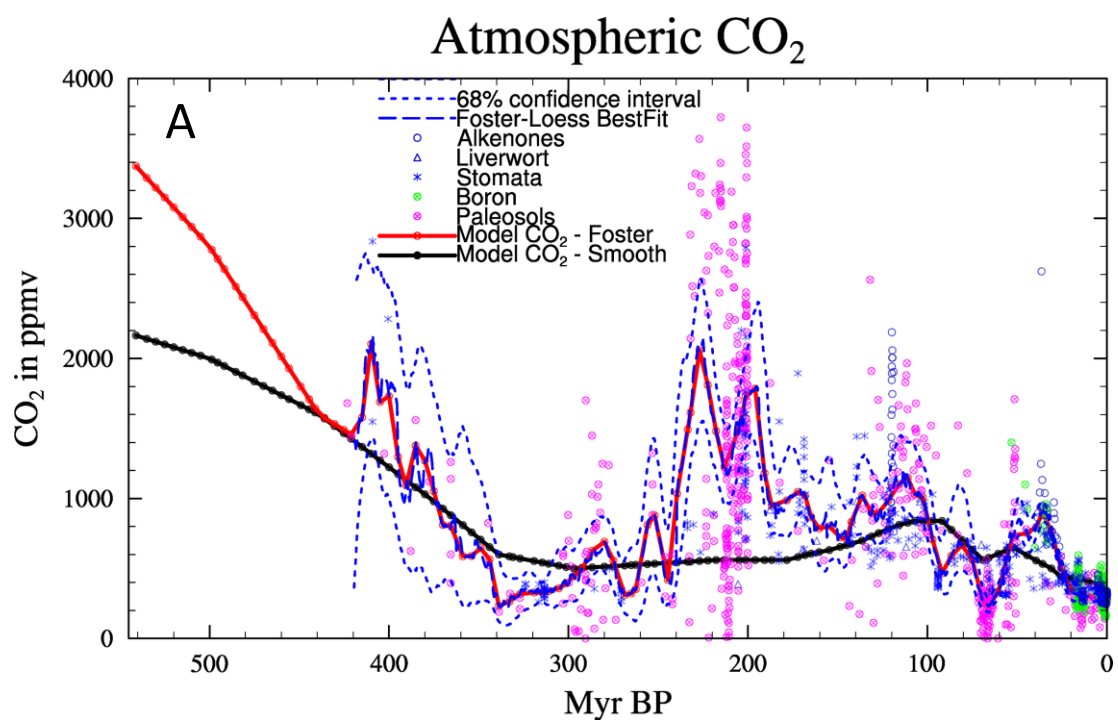
735

736

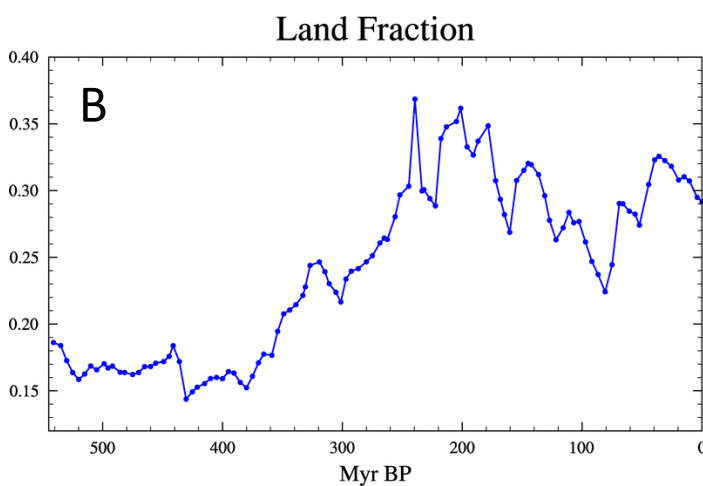


737 Figures

738 **Figure 1.** Summary of boundary condition changes to model of the Phanerozoic, (a) CO<sub>2</sub>  
739 reconstructions (from Foster et al. 2017) and the two scenarios used in the models, (b) Land-sea  
740 fraction from the paleogeographic reconstructions, and (c) land ice area input into model. The  
741 paleogeographic reconstructions can be accessed at [https://www.earthbyte.org/paleodem-](https://www.earthbyte.org/paleodem-resource-scotese-and-wright-2018/)  
742 [resource-scotese-and-wright-2018/](https://www.earthbyte.org/paleodem-resource-scotese-and-wright-2018/). An animation of the high-resolution (1° x 1°) and model  
743 resolution (3.75° longitude x 2.5° latitude) maps can be found here:  
744 [https://www.paleo.bristol.ac.uk/~ggpjv/scotese/scotese\\_raw\\_moll.normal\\_scotese\\_moll.normal.ht](https://www.paleo.bristol.ac.uk/~ggpjv/scotese/scotese_raw_moll.normal_scotese_moll.normal.ht)  
745 [ml](https://www.paleo.bristol.ac.uk/~ggpjv/scotese/scotese_raw_moll.normal_scotese_moll.normal.ht)

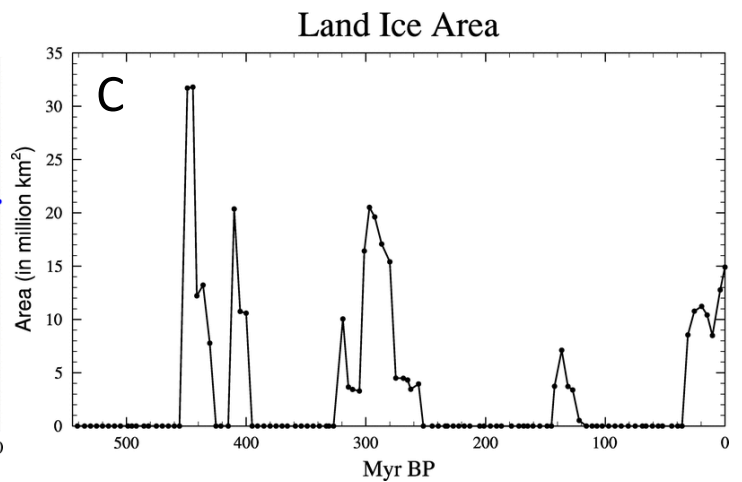


746



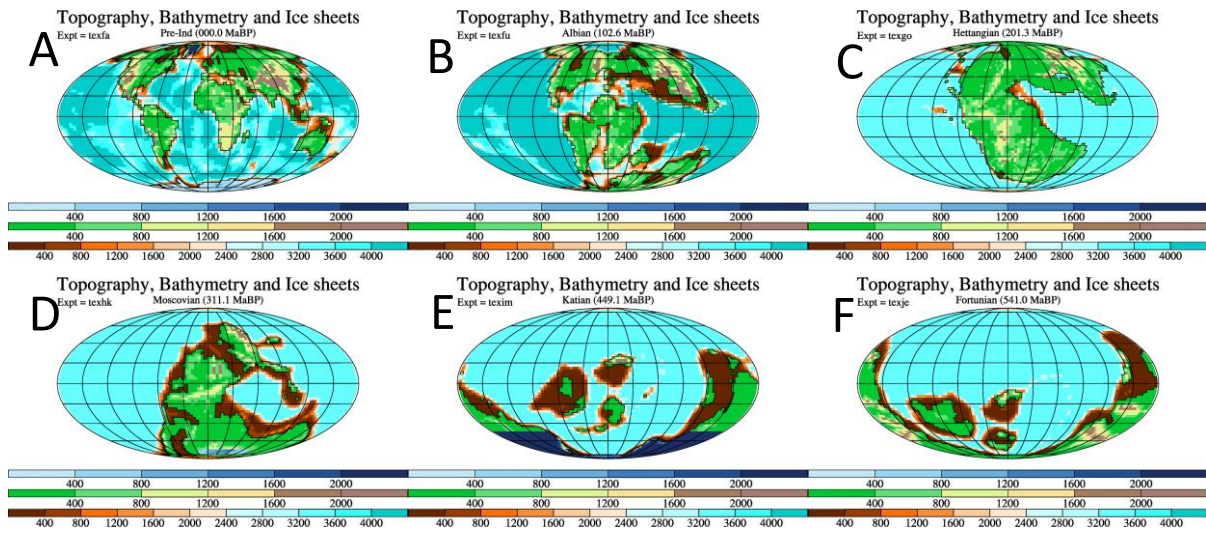
747

748



749 **Figure 2.** A few example paleogeographies, once they have been re-gridded onto the HadCM3L grid.  
 750 The examples are for (a) present day, (b) Albian, 102.6Ma (Lower Cretaceous), (c) Hettangian,  
 751 201.3Ma (lower Jurassic), (d) Moscovian, 311.1Ma (Pennsylvanian, Carboniferous), (e) Katian,  
 752 449.1Ma (Upper Ordovician), and (f) Fortunian, 541.0Ma (Cambrian). The top color legend refers to  
 753 the height of the ice sheets (if they exist), the middle color legend refers to heights on land (except  
 754 ice), and the lower color legend refers to the ocean bathymetry. All units are meters.

755



756

757

758

759

760

761

762

763

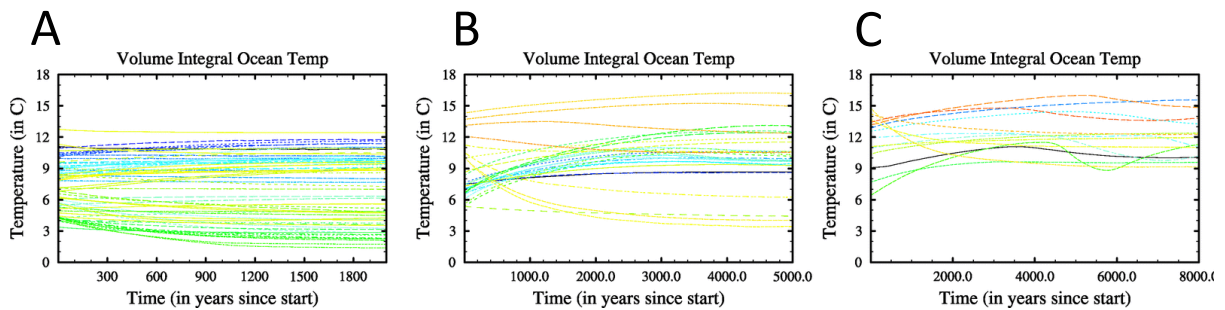
764

765

766

767 **Figure 3.** Time series of the annual, volume mean ocean temperature for all 109 simulations. (a)  
 768 shows those simulations for which 2000 years was sufficient to satisfy the convergence criteria  
 769 described in text (these were for all simulations listed in table 1 except those listed in (b) and (c)), (b)  
 770 those simulation which required 5000 years (these were for all the simulations for 31.0, 35.9, 39.5,  
 771 55.8, 60.6, 66.0, 69.0, 102.6, 107.0, 121.8, 127.2, 154.7, 160.4, 168.2, 172.2, 178.4, 186.8, 190.8,  
 772 196.0, 201.3, 204.9, 213.2, 217.8, 222.4, 227.0, 232.0, and 233.6 Ma BP), and (c) those simulation  
 773 which required 8000 years (these were simulations for 44.5, 52.2, 86.7, 91.9, 97.2, 111.0, 115.8,  
 774 131.2, 136.4, 142.4, 145.0, 148.6, 164.8, and 239.5 Ma BP). The different coloured lines show the  
 775 different runs. The plot simply show the extent to which all runs have reached steady state. For  
 776 more details about specific simulations, please see the supplementary figures.

777



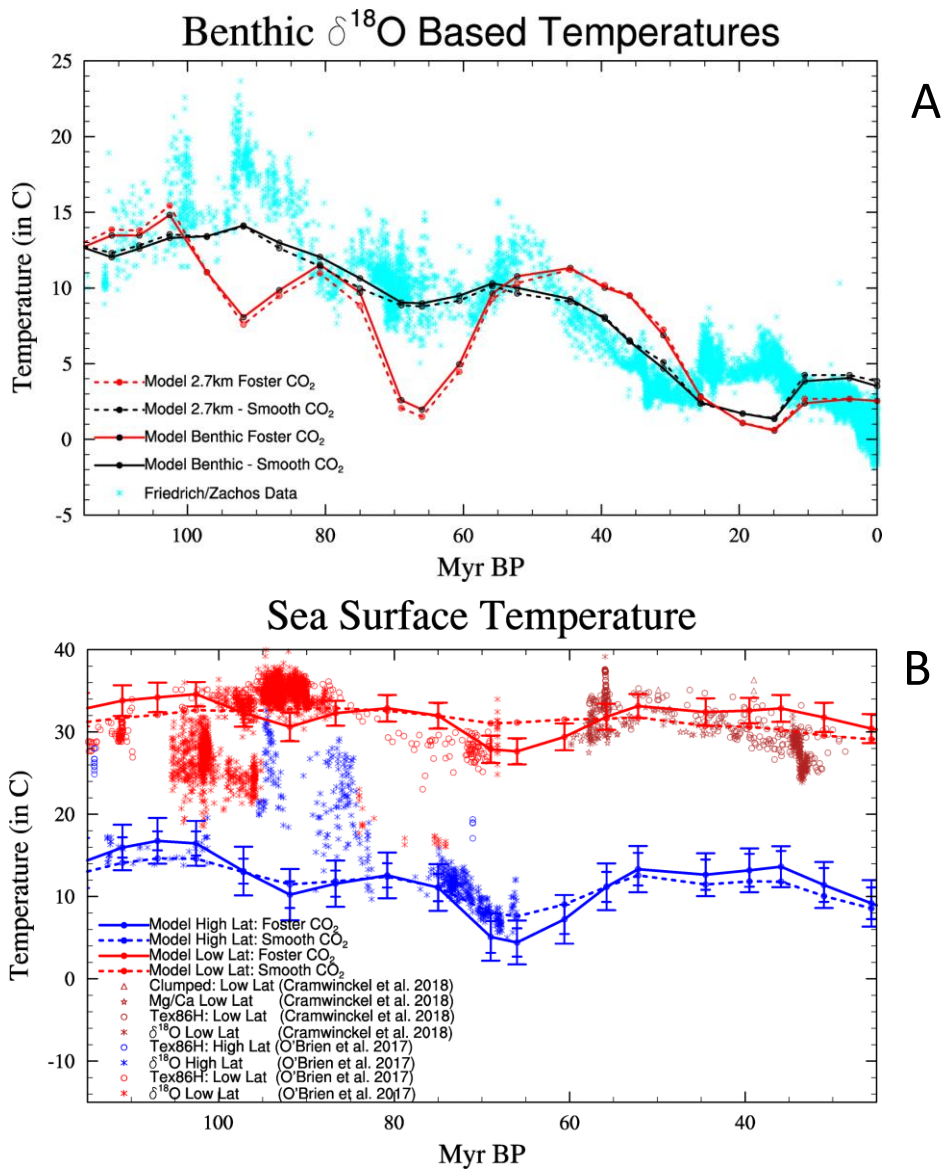
778

779

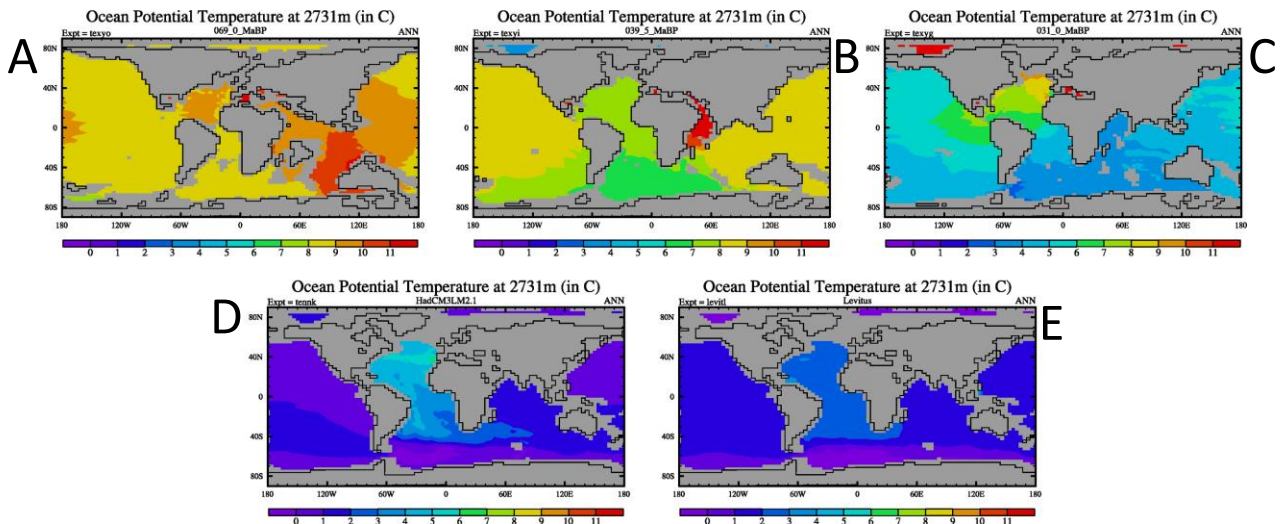
780

781 **Figure 4.** (a) Comparison of modelled deep ocean temperatures versus those from (Zachos et al.,  
 782 2008) and (Friedrich et al., 2012) converted to temperature using the formulation in (Hansen et al.,  
 783 2013). The model temperatures are global averages over the bottom layer of the model but excludes  
 784 shallow marine settings (less than 1000m). The dashed lines show the modelled global average  
 785 ocean temperatures at the model layer centered at 2731m, and (b) Comparison of modelled sea  
 786 surface temperatures with the compilations of (O'Brien et al., 2017) and (Cramwinckel et al., 2018).  
 787 The data is a combination of  $\text{Tex}_{86}$ ,  $\delta^{18}\text{O}$ , Mg/Ca, and clumped Isotope data. The model data shows  
 788 low latitude temperatures (averaged from 10S to 10N) and high latitude temperatures (averaged  
 789 over 47.5N to 65N and 47.5S to 65S). The Foster- $\text{CO}_2$  simulations also show a measure of the spatial  
 790 variability. The large bars show the spatial standard deviation across the whole region, and the  
 791 smaller bars shows the average spatial standard deviation along longitudes within the region. Note  
 792 that the ranges of both the x and y-axis differ between (a) and (b).

793



794 **Figure 5.** Modelled annual mean ocean temperatures are 2731m depth for three example past time  
 795 periods. The left figure is for the late Cretaceous, the center for the late Eocene (39.5Ma), and the  
 796 right for the Oligocene (31Ma). These are results from the smooth-CO<sub>2</sub> set of simulations which  
 797 agree better with the observed benthic temperature data. Also included are the pre-industrial  
 798 simulation and World Ocean Atlas 1994 observational data, provided by the NOAA-ESRL Physical  
 799 Sciences Laboratory, Boulder Colorado from their web site at <https://psl.noaa.gov/>. The thin black  
 800 lines show the coastlines, and the grey areas are showing where the ocean is shallower than 2731m.

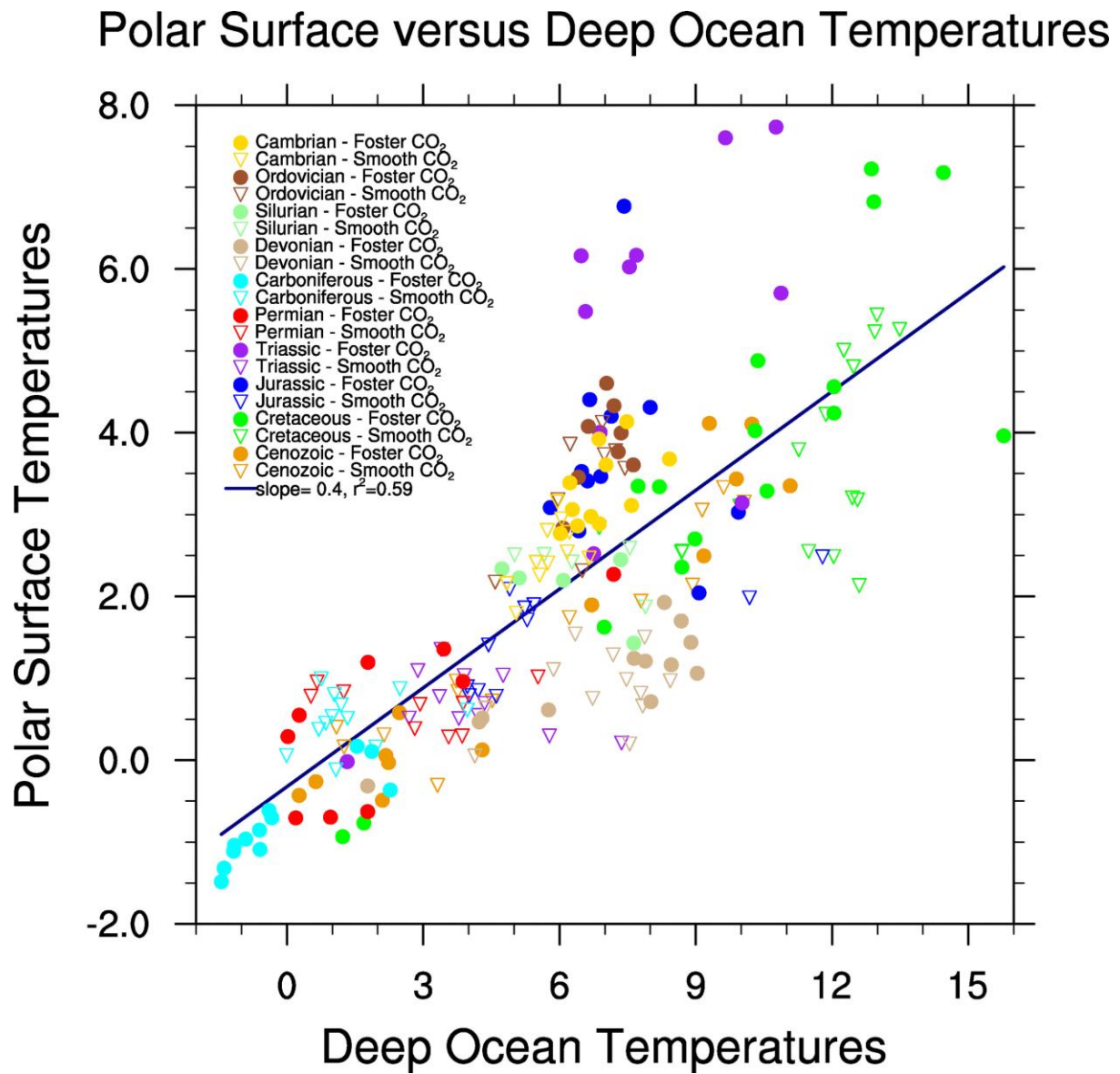


801

802



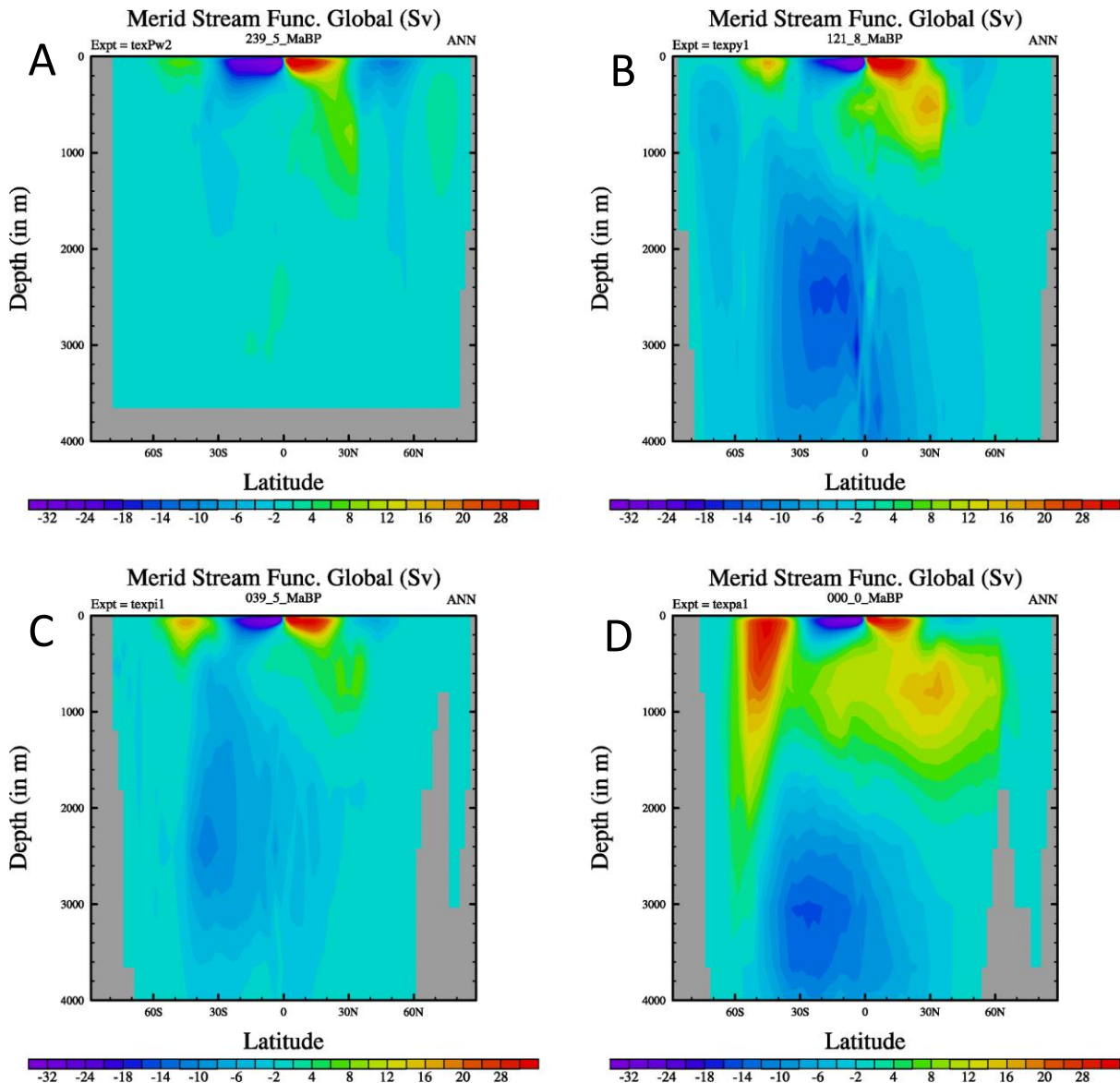
803 **Figure 6.** Correlations between deep ocean temperatures and surface polar sea surface  
 804 temperatures. The deep ocean temperatures are defined as the average temperature at the bottom  
 805 of the model ocean, where the bottom must be deeper than 1000m. The polar sea surface  
 806 temperatures are the average winter (i.e. northern polar in DJF and southern polar in JJA) sea  
 807 surface temperature polewards of 60°. The inverted triangles show the results from the smooth CO<sub>2</sub>  
 808 simulations and the dots refer to the Foster CO<sub>2</sub> simulations. The colors refer to different geological  
 809 era.



810

811 **Figure 7.** Global Ocean overturning circulation (in Sverdrup) for four different time periods for the  
 812 Foster-CO<sub>2</sub> simulations. Positive (yellow/red) values correspond to a clockwise circulation, negative  
 813 (dark blue/purple) values represent an anti-clockwise circulation. (a) Middle Triassic, Ladinian,  
 814 239.5Ma, (b) Lower Cretaceous, Aptian, 121.8 Ma, (c) Late Eocene, Bartonian, 39.5Ma, and (d)  
 815 Present Day. Paleogeographic reconstructions older than the oldest ocean floor (~Late-Jurassic) have  
 816 uniform deep ocean floor depth.

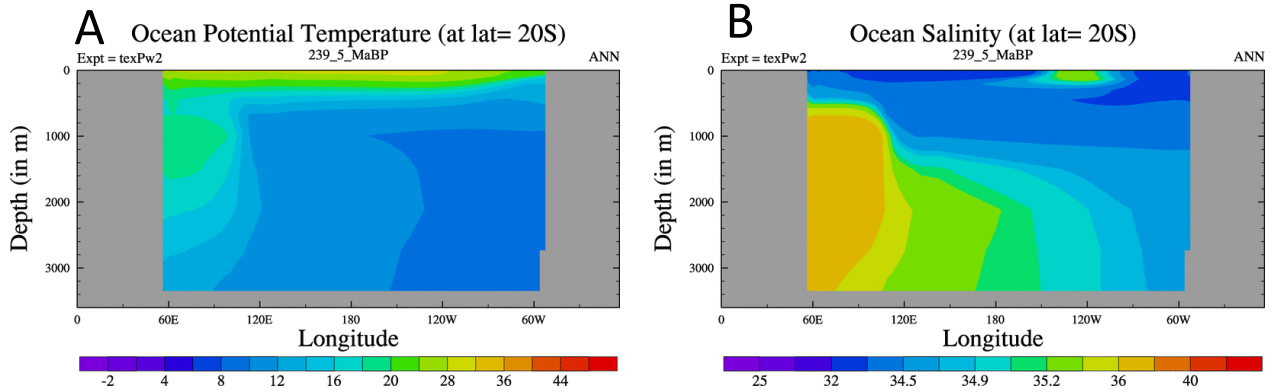
817



818

819

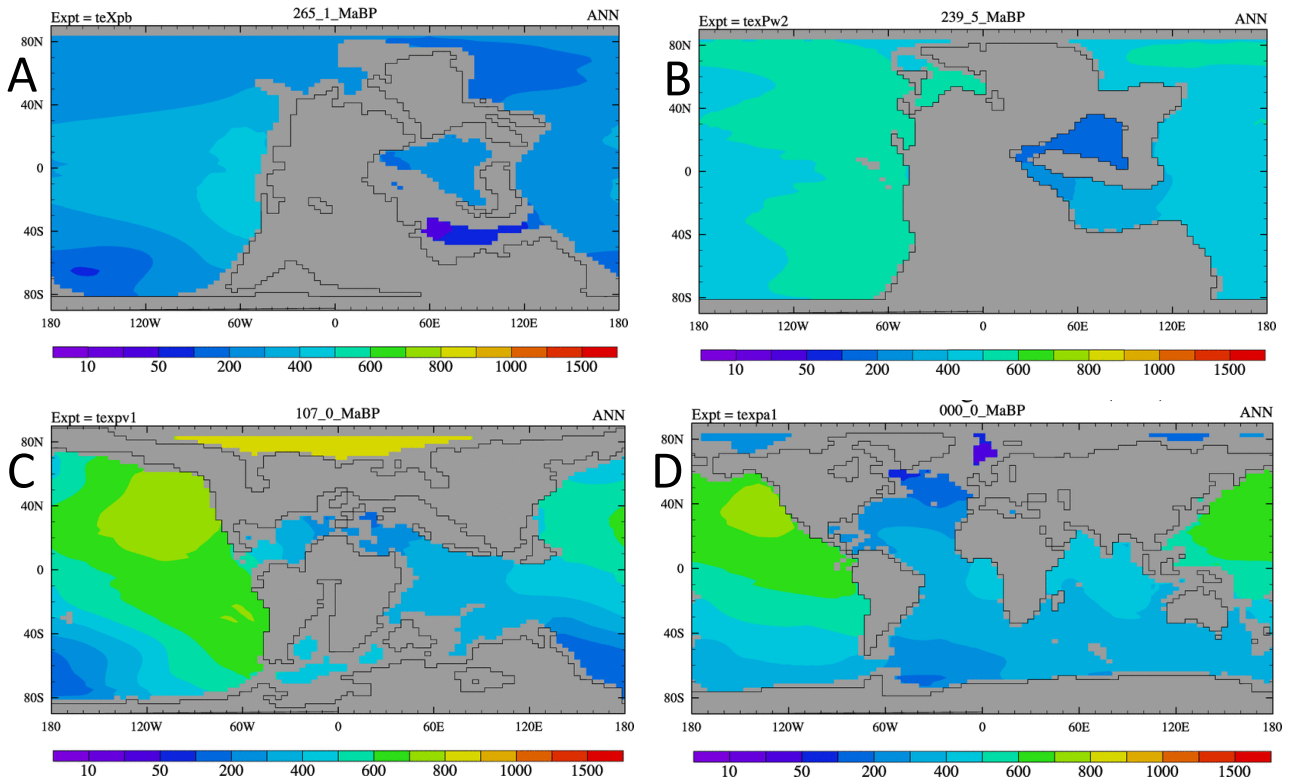
820 **Figure 8.** Longitudinal cross section at 20S of (a) ocean potential temperature and (b) salinity for the  
821 Ladanian (240Ma). Temperature is in C and salinity is in PSU.  
822  
823



824  
825  
826



827 **Figure 9.** Modelled age of water tracer at 2731m for 4 different time periods (a) 265Ma, (b) 240Ma,  
828 (c) 107Ma, and (d) 0Ma. Units are years.  
829

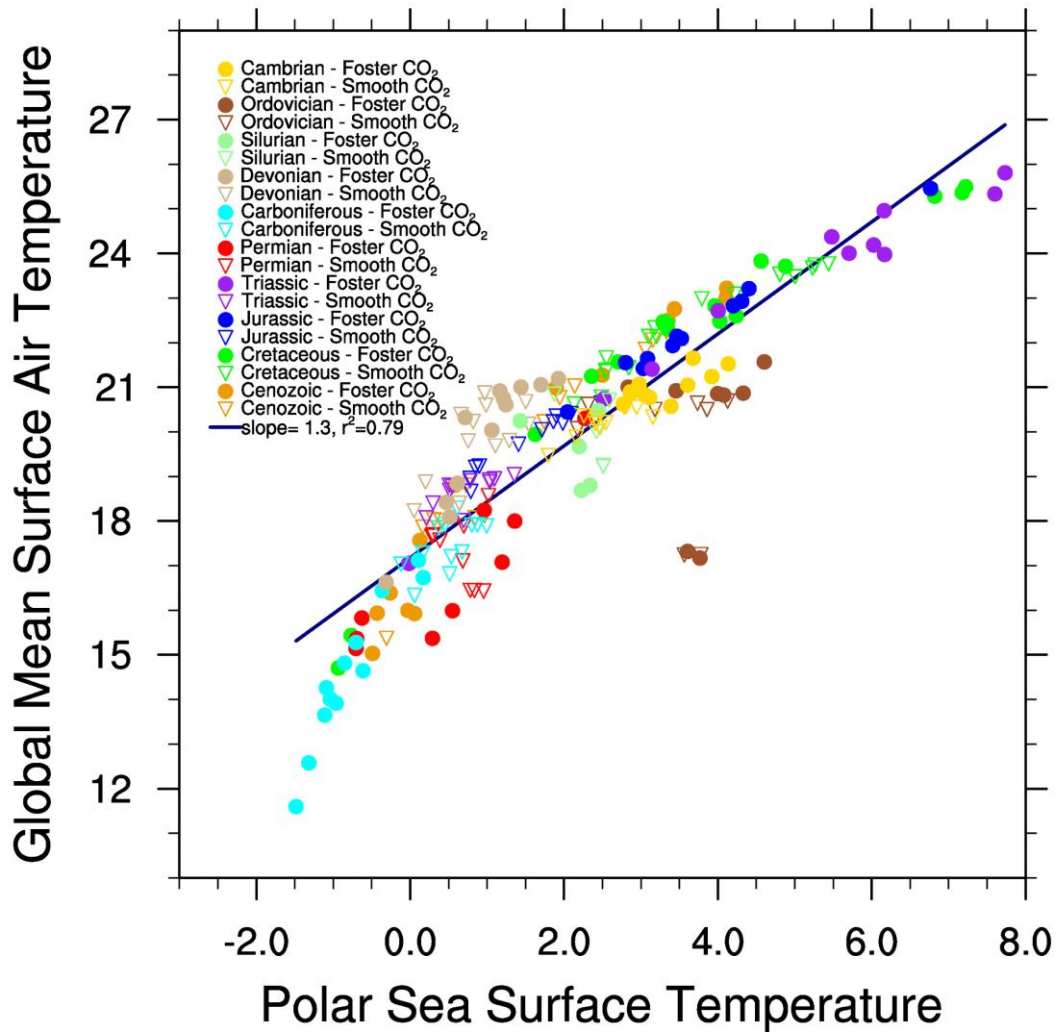


836 **Figure 10.** Correlation between high latitude ocean temperatures (polewards of 60°) and the annual  
837 mean, global mean surface air temperature. The polar temperatures are the average of the two  
838 winter hemispheres (i.e. northern DJF and southern JJA). Other details as in figure 6.

839

840

## Global Mean Surface Air Temperature versus Polar SST

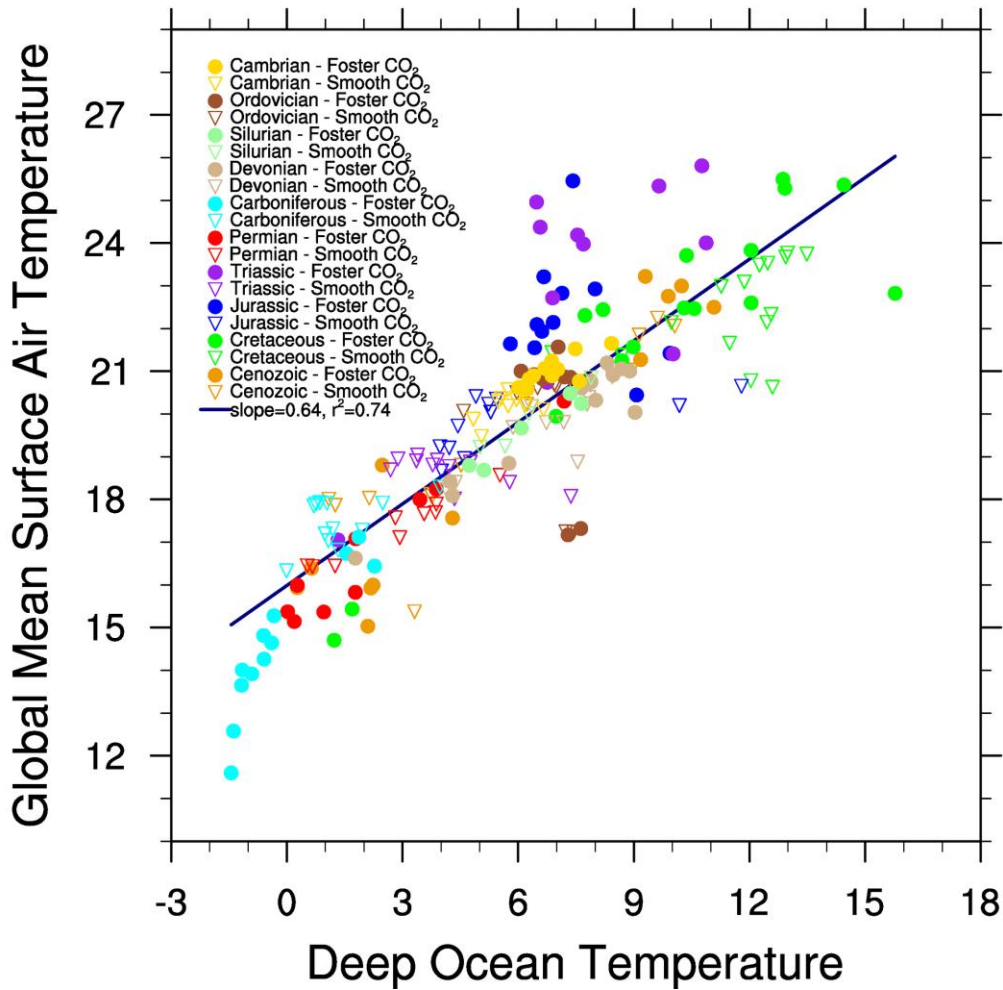


841

842 **Figure 11.** Correlation between the global mean, annual mean surface air temperature and the deep  
843 ocean temperature. The deep ocean temperatures are defined as the average temperature at the  
844 bottom of the model ocean, where the bottom must be deeper than 1000m. Other details as in  
845 figure 6.

846

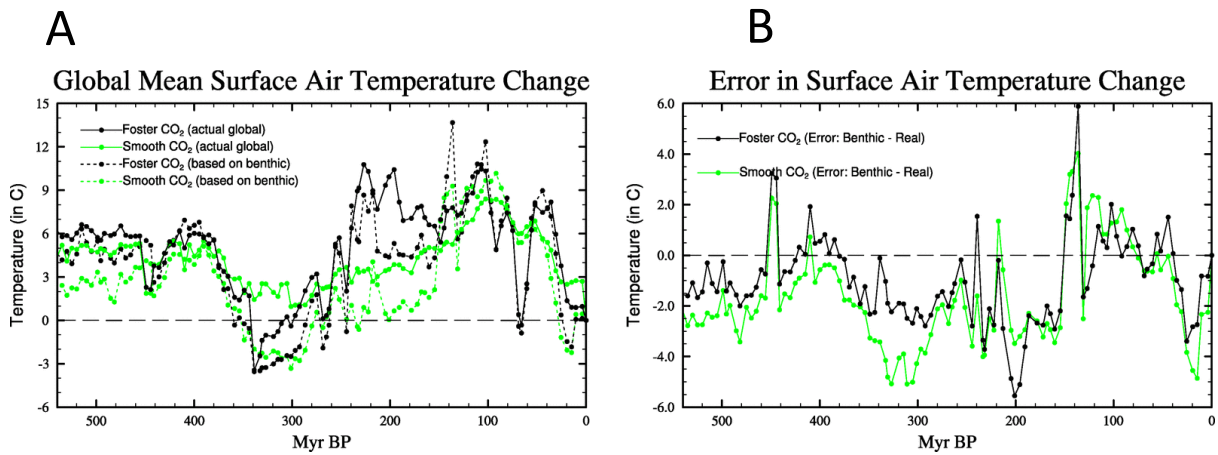
## Surface Air Temperature versus Deep Ocean Temperature



847

848

849 **Figure 12.** Phanerozoic Time series of modelled temperature change (relative to pre-Industrial) for  
 850 the smooth (green lines) and Foster-CO<sub>2</sub> (black) simulations (a) shows the actual modelled global  
 851 mean surface air temperature (solid lines) whereas the dashed line shows the estimate based on  
 852 deep ocean temperatures, and (b) error in the estimate of global mean temperature change if based  
 853 on deep ocean temperatures (i.e. deep ocean – global mean surface temperatures).  
 854



855 References

- 856 Alexeev, V.A., Langen, P.L., Bates, J.R., 2005. Polar amplification of surface warming on an  
857 aquaplanet in "ghost forcing" experiments without sea ice feedbacks. *Clim. Dyn.* 24, 655-666.
- 858 Baatsen, M., van Hinsbergen, D.J.J., von der Heydt, A.S., Dijkstra, H.A., Sluijs, A., Abels, H.A., Bijl, P.K.,  
859 2016. Reconstructing geographical boundary conditions for palaeoclimate modelling during the  
860 Cenozoic. *Clim. Past.* 12, 1635-1644.
- 861 Baatsen, M.L.J., von der Heydt, A.S., Kliphuis, M., Viebahn, J., Dijkstra, H.A., 2018. Multiple states in  
862 the late Eocene ocean circulation. *Glob. Planet. Change* 163, 18-28.
- 863 Barron, E.J., Peterson, W.H., 1990. MID-CRETACEOUS OCEAN CIRCULATION: RESULTS FROM MODEL  
864 SENSITIVITY STUDIES. *Paleoceanography* 5, 319-337.
- 865 Beerling, D.J., Fox, A., Stevenson, D.S., Valdes, P.J., 2011. Enhanced chemistry-climate feedbacks in  
866 past greenhouse worlds. *P Natl Acad Sci USA* 108, 9770-9775.
- 867 Bjerknes, J., 1964. Atlantic Air-Sea Interaction, in: Landsberg, H.E., Van Mieghem, J. (Eds.), 0065-  
868 2687. Elsevier, pp. 1-82.
- 869 Brass, G.W., Southam, J.R., Peterson, W.H., 1982. Warm Saline Bottom Water in the Ancient Ocean.  
870 *Nature* 296, 620-623.
- 871 Cramer, B.S., Toggweiler, J.R., Wright, J.D., Katz, M.E., Miller, K.G., 2009. Ocean overturning since the  
872 Late Cretaceous: Inferences from a new benthic foraminiferal isotope compilation.  
873 *Paleoceanography* 24.
- 874 Cramwinckel, M.J., Huber, M., Kocken, I.J., Agnini, C., Bijl, P.K., Bohaty, S.M., Frieling, J., Goldner, A.,  
875 Hilgen, F.J., Kip, E.L., Peterse, F., van der Ploeg, R., Rohl, U., Schouten, S., Sluijs, A., 2018.  
876 Synchronous tropical and polar temperature evolution in the Eocene. *Nature* 559, 382-+.
- 877 Dietmuller, S., Ponater, M., Sausen, R., 2014. Interactive ozone induces a negative feedback in CO<sub>2</sub>-  
878 driven climate change simulations. *J. Geophys. Res.-Atmos.* 119, 1796-1805.
- 879 Donnadieu, Y., Puceat, E., Moiroud, M., Guillocheau, F., Deconinck, J.F., 2016. A better-ventilated  
880 ocean triggered by Late Cretaceous changes in continental configuration. *Nat Commun* 7, 12.
- 881 Emiliani, C., 1954. Temperatures of Pacific Bottom Waters and Polar Superficial Waters during the  
882 Tertiary. *Science* 119, 853-855.
- 883 England, M.H., 1995. The Age Of Water And Ventilation Timescales In A Global Ocean Model. *J Phys*  
884 *Oceanogr* 25, 2756-2777.
- 885 Farnsworth, A., Lunt, D.J., O'Brien, C.L., Foster, G.L., Inglis, G.N., Markwick, P., Pancost, R.D.,  
886 Robinson, S.A., 2019a. Climate Sensitivity on Geological Timescales Controlled by Nonlinear  
887 Feedbacks and Ocean Circulation. *Geophys. Res. Lett.* 46, 9880-9889.
- 888 Farnsworth, A., Lunt, D.J., Robinson, S.A., Valdes, P.J., Roberts, W.H.G., Clift, P.D., Markwick, P., Su,  
889 T., Wrobel, N., Bragg, F., Kelland, S.J., Pancost, R.D., 2019b. Past East Asian monsoon evolution  
890 controlled by paleogeography, not CO<sub>2</sub>. *Sci Adv* 5.
- 891 Foster, G.L., Royer, D.L., Lunt, D.J., 2017. Future climate forcing potentially without precedent in the  
892 last 420 million years. *Nat Commun* 8.
- 893 Friedrich, O., Norris, R.D., Erbacher, J., 2011. Evolution of Cretaceous oceans: A 55 million year  
894 record of Earth's temperature and carbon cycle. *Grzyb Found Spec Pub* 17, 85-85.
- 895 Friedrich, O., Norris, R.D., Erbacher, J., 2012. Evolution of middle to Late Cretaceous oceans-A 55  
896 m.y. record of Earth's temperature and carbon cycle. *Geology* 40, 107-110.
- 897 Goldner, A., Herold, N., Huber, M., 2014. The challenge of simulating the warmth of the mid-  
898 Miocene climatic optimum in CESM1. *Clim. Past.* 10, 523-536.
- 899 Gordon, C., Cooper, C., Senior, C.A., Banks, H., Gregory, J.M., Johns, T.C., Mitchell, J.F.B., Wood, R.A.,  
900 2000. The simulation of SST, sea ice extents and ocean heat transports in a version of the Hadley  
901 Centre coupled model without flux adjustments. *Clim. Dyn.* 16, 147-168.
- 902 Gough, D.O., 1981. Solar Interior Structure and Luminosity Variations. *Sol Phys* 74, 21-34.

903 Gregory, J.M., Ingram, W.J., Palmer, M.A., Jones, G.S., Stott, P.A., Thorpe, R.B., Lowe, J.A., Johns,  
904 T.C., Williams, K.D., 2004. A new method for diagnosing radiative forcing and climate sensitivity.  
905 *Geophys. Res. Lett.* 31.

906 Hansen, J., Sato, M., Kharecha, P., Beerling, D., Berner, R., Masson-Delmotte, V., Pagani, M., Raymo,  
907 M., Royer, D.L., Zachos, J.C., 2008. Target atmospheric CO<sub>2</sub>: Where should humanity aim? *Open*  
908 *Atmos. Sci. J.* 2, 217-231.

909 Hansen, J., Sato, M., Russell, G., Kharecha, P., 2013. Climate sensitivity, sea level and atmospheric  
910 carbon dioxide. *Philos T R Soc A* 371.

911 Hansen, J.E., Sato, M., 2012. *Paleoclimate Implications for Human-Made Climate Change*. Springer  
912 Vienna, Vienna, pp. 21-47.

913 Hardiman, S.C., Andrews, M.B., Andrews, T., Bushell, A.C., Dunstone, N.J., Dyson, H., Jones, G.S.,  
914 Knight, J.R., Neinger, E., O'Connor, F.M., Ridley, J.K., Ringer, M.A., Scaife, A.A., Senior, C.A., Wood,  
915 R.A., 2019. The Impact of Prescribed Ozone in Climate Projections Run With HadGEM3-GC3.1. *J Adv*  
916 *Model Earth Sy* 11, 3443-3453.

917 Harris, J., Ashley, A., Otto, S., Valdes, P., Crossley, R., Preston, R., Watson, J., Goodrich, M., Team.,  
918 M.P., 2017. Paleogeography and Paleo-Earth Systems in the Modeling of Marine Paleoproductivity: A  
919 Prerequisite for the Prediction of Petroleum Source Rocks, in: Mahdi A. AbuAli, I.M., and Hege M.  
920 Nordgård Bolås (Ed.), *Petroleum Systems Analysis—Case Studies*. AAPG Memoir, pp. 27-60.

921 Henkes, G.A., Passey, B.H., Grossman, E.L., Shenton, B.J., Yancey, T.E., Perez-Huerta, A., 2018.  
922 Temperature evolution and the oxygen isotope composition of Phanerozoic oceans from carbonate  
923 clumped isotope thermometry. *Earth Planet. Sci. Lett.* 490, 40-50.

924 Holland, M.M., Bitz, C.M., 2003. Polar amplification of climate change in coupled models. *Clim. Dyn.*  
925 21, 221-232.

926 Kageyama, M., Albani, S., Braconnot, P., Harrison, S.P., Hopcroft, P.O., Ivanovic, R.F., Lambert, F.,  
927 Marti, O., Peltier, W.R., Peterschmitt, J.Y., Roche, D.M., Tarasov, L., Zhang, X., Brady, E.C., Haywood,  
928 A.M., LeGrande, A.N., Lunt, D.J., Mahowald, N.M., Mikolajewicz, U., Nisancioglu, K.H., Otto-Bliesner,  
929 B.L., Renssen, H., Tomas, R.A., Zhang, Q., Abe-Ouchi, A., Bartlein, P.J., Cao, J., Li, Q., Lohmann, G.,  
930 Ohgaito, R., Shi, X.X., Volodin, E., Yoshida, K., Zhang, X., Zheng, W.P., 2017. The PMIP4 contribution  
931 to CMIP6-Part 4: Scientific objectives and experimental design of the PMIP4-CMIP6 Last Glacial  
932 Maximum experiments and PMIP4 sensitivity experiments. *Geosci Model Dev* 10, 4035-4055.

933 Kennett, J.P., Stott, L.D., 1991. Abrupt Deep-Sea Warming, Palaeoceanographic Changes and Benthic  
934 Extinctions at the End of the Paleocene. *Nature* 353, 225-229.

935 Kiehl, J.T., Shields, C.A., 2013. Sensitivity of the Palaeocene-Eocene Thermal Maximum climate to  
936 cloud properties. *Philos T R Soc A* 371.

937 Knorr, G., Butzin, M., Micheels, A., Lohmann, G., 2011. A warm Miocene climate at low atmospheric  
938 CO<sub>2</sub> levels. *Geophys. Res. Lett.* 38, 5.

939 Krapp, M., Jungclaus, J.H., 2011. The Middle Miocene climate as modelled in an atmosphere-ocean-  
940 biosphere model. *Clim. Past.* 7, 1169-1188.

941 Ladant, J.B., Poulsen, C.J., Fluteau, F., Tabor, C.R., MacLeod, K.G., Martin, E.E., Haynes, S.J., Rostami,  
942 M.A., 2020. Paleogeographic controls on the evolution of Late Cretaceous ocean circulation. *Clim.*  
943 *Past.* 16, 973-1006.

944 Lunt, D.J., Bragg, F., Chan, W.L., Hutchinson, D.K., Ladant, J.B., Morozova, P., Niezgodzki, I., Steinig,  
945 S., Zhang, Z., Zhu, J., Abe-Ouchi, A., Anagnostou, E., de Boer, A.M., Coxall, H.K., Donnadieu, Y.,  
946 Foster, G., Inglis, G.N., Knorr, G., Langebroek, P.M., Lear, C.H., Lohmann, G., Poulsen, C.J., Sepulchre,  
947 P., Tierney, J.E., Valdes, P.J., Volodin, E.M., Dunkley Jones, T., Hollis, C.J., Huber, M., Otto-Bliesner,  
948 B.L., 2021. DeepMIP: model intercomparison of early Eocene climatic optimum (EECO) large-scale  
949 climate features and comparison with proxy data. *Clim. Past* 17, 203-227.

950 Lunt, D.J., Dunkley Jones, T., Heinemann, M., Huber, M., LeGrande, A., Winguth, A., Loptson, C.,  
951 Marotzke, J., Roberts, C.D., Tindall, J., Valdes, P., Winguth, C., 2012. A model-data comparison for a  
952 multi-model ensemble of early Eocene atmosphere-ocean simulations: EoMIP. *Clim. Past.* 8, 1717-  
953 1736.

954 Lunt, D.J., Farnsworth, A., Loptson, C., Foster, G.L., Markwick, P., O'Brien, C.L., Pancost, R.D.,  
955 Robinson, S.A., Wrobel, N., 2016. Palaeogeographic controls on climate and proxy interpretation.  
956 *Clim. Past.* 12, 1181-1198.

957 Lunt, D.J., Huber, M., Anagnostou, E., Baatsen, M.L.J., Caballero, R., DeConto, R., Dijkstra, H.A.,  
958 Donnadieu, Y., Evans, D., Feng, R., Foster, G.L., Gasson, E., von der Heydt, A.S., Hollis, C.J., Inglis,  
959 G.N., Jones, S.M., Kiehl, J., Turner, S.K., Korty, R.L., Kozdon, R., Krishnan, S., Ladant, J.B., Langebroek,  
960 P., Lear, C.H., LeGrande, A.N., Littler, K., Markwick, P., Otto-Bliesner, B., Pearson, P., Poulsen, C.J.,  
961 Salzmann, U., Shields, C., Snell, K., Starz, M., Super, J., Tabor, C., Tierney, J.E., Tourte, G.J.L., Tripathi,  
962 A., Upchurch, G.R., Wade, B.S., Wing, S.L., Winguth, A.M.E., Wright, N.M., Zachos, J.C., Zeebe, R.E.,  
963 2017. The DeepMIP contribution to PMIP4: experimental design for model simulations of the EECO,  
964 PETM, and pre-PETM (version 1.0). *Geosci Model Dev* 10, 889-901.

965 Lunt, D.J., Valdes, P.J., Dunkley Jones, T., Ridgwell, A., Haywood, A.M., Schmidt, D.N., Marsh, R.,  
966 Maslin, M., 2010. CO<sub>2</sub>-driven ocean circulation changes as an amplifier of Paleocene-Eocene thermal  
967 maximum hydrate destabilization. *Geology* 38, 875-878.

968 Murphy, D.P., Thomas, D.J., 2012. Cretaceous deep-water formation in the Indian sector of the  
969 Southern Ocean. *Paleoceanography* 27.

970 Nowack, P.J., Abraham, N.L., Maycock, A.C., Braesicke, P., Gregory, J.M., Joshi, M.M., Osprey, A.,  
971 Pyle, J.A., 2015. A large ozone-circulation feedback and its implications for global warming  
972 assessments. *Nat Clim Change* 5, 41-45.

973 Nunes, F., Norris, R.D., 2006. Abrupt reversal in ocean overturning during the Palaeocene/Eocene  
974 warm period. *Nature* 439, 60-63.

975 O'Brien, C.L., Robinson, S.A., Pancost, R.D., Damste, J.S.S., Schouten, S., Lunt, D.J., Alsenz, H.,  
976 Bomemann, A., Bottini, C., Brassell, S.C., Farnsworth, A., Forster, A., Huber, B.T., Inglis, G.N., Jenkyns,  
977 H.C., Linnert, C., Littler, K., Markwick, P., McAnena, A., Mutterlose, J., Naafs, B.D.A., Puttmann, W.,  
978 Sluijs, A., van Helmond, N.A.G.M., Vellekoop, J., Wagner, T., Wrobel, N.E., 2017. Cretaceous sea-  
979 surface temperature evolution: Constraints from TEX86 and planktonic foraminiferal oxygen  
980 isotopes. *0012-8252* 172, 224-247.

981 Outten, S., Esau, I., Ottera, O.H., 2018. Bjerknes Compensation in the CMIP5 Climate Models. *J. Clim.*  
982 31, 8745-8760.

983 Pope, V.D., Gallani, M.L., Rowntree, P.R., Stratton, R.A., 2000. The impact of new physical  
984 parametrizations in the Hadley Centre climate model: HadAM3. *Clim. Dyn.* 16, 123-146.

985 Poulsen, C.J., Barron, E.J., Arthur, M.A., Peterson, W.H., 2001. Response of the mid-Cretaceous  
986 global oceanic circulation to tectonic and CO<sub>2</sub> forcings. *Paleoceanography* 16, 576-592.

987 Sagoo, N., Valdes, P., Flecker, R., Gregoire, L.J., 2013. The Early Eocene equable climate problem: can  
988 perturbations of climate model parameters identify possible solutions? *Philos T R Soc A* 371.

989 Scotese, C.R., 2016. PALEOMAP PaleoAtlas for GPLates and the PaleoData Plotter Program,  
990 PALEOMAP Project, <http://www.earthbyte.org/paleomap-paleoatlas-for-gplates/>.

991 Scotese, C.R., Schettino, A., 2017. Late Permian – Early Jurassic Paleogeography of Western Tethys  
992 and the World, in: Soto, J.I., Flinch, J., Tari, G. (Eds.), *Permo-Triassic Salt Provinces of Europe, North  
993 Africa and the Atlantic Margins*. Elsevier, pp. 57-95.

994 Scotese, C.R., Wright, N., 2018. PALEOMAP Paleodigital Elevation MOdels (PaleoDEMS) for the  
995 Phanerozoic, PALEOMAP Project, <https://www.earthbyte.org/paleodem-resource-scotese-and-wright-2018/>.

996

997 Smith, R.S., Gregory, J.M., Osprey, A., 2008. A description of the FAMOUS (version XDBUA) climate  
998 model and control run. *Geosci Model Dev* 1, 53-68.

999 Song, H.J., Wignall, P.B., Song, H.Y., Dai, X., Chu, D.L., 2019. Seawater Temperature and Dissolved  
1000 Oxygen over the Past 500 Million Years. *J Earth Sci-China* 30, 236-243.

1001 Steinthorsdottir, M., H. K. Coxall, A. M. de Boer, M. Huber, N. Barbolini, C. D. Bradshaw, N. J. Burls, S.  
1002 J. Feakins, E. Gasson, J. Henderiks, A. Holbourn, S. Kiel, M. J. Kohn, G. Knorr, W. M. Kurschner, C. H.  
1003 Lear, D. Liebrand, D. J. Lunt, T. Mors, P. N. Pearson, M. J. Pound, H. Stoll, C. A. E. Stromberg, 2021.  
1004 The Miocene: the Future of the Past. *Paleoceanography and Paleoclimatology*. In press.

1005 Stoll, H.M., Guitian, J., Hernandez-Almeida, I., Mejia, L.M., Phelps, S., Polissar, P., Rosenthal, Y.,  
1006 Zhang, H.R., Ziveri, P., 2019. Upregulation of phytoplankton carbon concentrating mechanisms  
1007 during low CO<sub>2</sub> glacial periods and implications for the phytoplankton pCO<sub>2</sub> proxy. *Quat. Sci. Rev.*  
1008 208, 1-20.

1009 Sutton, R.T., Dong, B.W., Gregory, J.M., 2007. Land/sea warming ratio in response to climate change:  
1010 IPCC AR4 model results and comparison with observations. *Geophys. Res. Lett.* 34.

1011 Upchurch, G.R., Kiehl, J., Shields, C., Scherer, J., Scotese, C., 2015. Latitudinal temperature gradients  
1012 and high-latitude temperatures during the latest Cretaceous: Congruence of geologic data and  
1013 climate models. *Geology* 43, 683-686.

1014 **Valdes, P.J.**, Armstrong, E., Badger, M.P.S., Bradshaw, C.D., Bragg, F., Crucifix, M., Davies-Barnard, T.,  
1015 Day, J.J., Farnsworth, A., Gordon, C., Hopcroft, P.O., Kennedy, A.T., Lord, N.S., Lunt, D.J., Marzocchi,  
1016 A., Parry, L.M., Pope, V., Roberts, W.H.G., Stone, E.J., Tourte, G.J.L., Williams, J.H.T., 2017. The  
1017 BRIDGE HadCM3 family of climate models: HadCM3@Bristol v1.0. *Geosci Model Dev* 10, 3715-3743.

1018 Verard, C., Hochard, C., Baumgartner, P.O., Stampfli, G.M., 2015. 3D palaeogeographic  
1019 reconstructions of the Phanerozoic versus sea-level and Sr-ratio variations. *J Palaeogeog-English* 4,  
1020 64-84.

1021 Witkowski, C.R., Weijers, J.W.H., Blais, B., Schouten, S., Damste, J.S.S., 2018. Molecular fossils from  
1022 phytoplankton reveal secular Pco<sub>2</sub> trend over the Phanerozoic. *Sci Adv* 4.

1023 You, Y., Huber, M., Muller, R.D., Poulsen, C.J., Ribbe, J., 2009. Simulation of the Middle Miocene  
1024 Climate Optimum. *Geophys. Res. Lett.* 36.

1025 Zachos, J., Pagani, M., Sloan, L., Thomas, E., Billups, K., 2001. Trends, rhythms, and aberrations in  
1026 global climate 65 Ma to present. *Science* 292, 686-693.

1027 Zachos, J.C., Dickens, G.R., Zeebe, R.E., 2008. An early Cenozoic perspective on greenhouse warming  
1028 and carbon-cycle dynamics. *Nature* 451, 279-283.

1029 Zhou, J., Poulsen, C.J., Pollard, D., White, T.S., 2008. Simulation of modern and middle Cretaceous  
1030 marine delta O-18 with an ocean-atmosphere general circulation model. *Paleoceanography* 23, 11.

1031 Zhu, J., Poulsen, C.J., Tierney, J.E., 2019. Simulation of Eocene extreme warmth and high climate  
1032 sensitivity through cloud feedbacks. *Sci Adv* 5.

1033

1034



Table I. List of Paleogeographic Maps and PaleoDEMs

Map Number	Stratigraphic Age Description	Plate Model Age
1	Present-day (Holocene, 0 Ma)	0
2	<i>Last Glacial Maximum (Pleistocene, 21 ky)*</i>	0
3	<i>Late Pleistocene (122 ky)*</i>	0
4	<i>Middle Pleistocene (454 ky)*</i>	0
5	<i>Early Pleistocene (Calabrian, 1.29 Ma)*</i>	0
6	<i>Early Pleistocene (Gelasian, 2.19)*</i>	0
7	Late Pliocene (Piacenzian, 3.09)	5
8	<i>Early Pliocene (Zanclean, 4.47 Ma)*</i>	5
9	<i>latest Miocene (Messinian, 6.3 Ma)*</i>	5
10	Middle/Late Miocene (Serravallian&Tortonian, 10.5 Ma)	10
11	Middle Miocene (Langhian, 14.9 Ma)	15
12	Early Miocene (Aquitanian&Burdigalian, 19.5 Ma)	20
13	Late Oligocene (Chattian, 25.6 Ma)	25
14	Early Oligocene (Rupelian, 31 Ma)	30
15	Late Eocene (Priabonian, 35.9 Ma)	35
16	late Middle Eocene (Bartonian, 39.5 Ma)	40
17	early Middle Eocene (Lutetian, 44.5 Ma)	45
18	Early Eocene (Ypresian, 51.9 Ma)	50
19	Paleocene/Eocene Boundary (PETM, 56 Ma)	55
20	Paleocene (Danian&Thanetian, 61 Ma)	60
21	KT Boundary (latest Maastrichtian, 66 Ma)	65
22	Late Cretaceous (Maastrichtian, 69 Ma)	70
23	Late Cretaceous (Late Campanian, 75 Ma)	75
24	Late Cretaceous (Early Campanian, 80.8 Ma)	80
25	Late Cretaceous (Santonian&Coniacian, 86.7 Ma)	85
26	Mid-Cretaceous (Turonian , 91.9 Ma)	90

27	Mid-Cretaceous (Cenomanian, 97.2 Ma)	95
28	Early Cretaceous (late Albian, 102.6 Ma)	100
29	Early Cretaceous (middle Albian, 107 Ma)	105
30	Early Cretaceous (early Albian, 111 Ma)	110
31	Early Cretaceous (late Aptian, 115.8 Ma)	115
32	Early Cretaceous (early Aptian, 121.8 Ma)	120
33	Early Cretaceous (Barremian, 127.2 Ma)	125
34	Early Cretaceous (Hauterivian, 131.2 Ma)	130
35	Early Cretaceous (Valanginian, 136.4 Ma)	135
36	Early Cretaceous (Berriasian, 142.4 Ma)	140
37	Jurassic/Cretaceous Boundary (145 Ma)	145
38	Late Jurassic (Tithonian, 148.6 Ma)	150
39	Late Jurassic (Kimmeridgian, 154.7 Ma)	155
40	Late Jurassic (Oxfordian, 160.4 Ma)	160
41	Middle Jurassic (Callovian, 164.8 Ma)	165
42	Middle Jurassic (Bajocian&Bathonian, 168.2)	170
43	Middle Jurassic (Aalenian, 172.2 Ma)	175
44	Early Jurassic (Toarcian, 178.4 Ma)	180
45	Early Jurassic (Pliensbachian, 186.8 Ma)	185
46	Early Jurassic (Sinemurian/Pliensbachian, 190.8 Ma)	190
47	Early Jurassic (Hettangian&Sinemurian, 196 Ma)	195
48	Late Triassic (Rhaetian/Hettangian, 201.3 Ma)	200
49	Late Triassic (Rhaetian, 204.9 Ma)	205
50	Late Triassic (late Norian, 213.2 Ma)	210
51	Late Triassic (mid Norian, 217.8 Ma)	215
52	Late Triassic (early Norian, 222.4 Ma)	220
53	Late Triassic (Carnian/Norian 227 Ma)	225
54	Late Triassic (Carnian, 232 Ma)	230

55	Late Triassic (early Carnian, 233.6)	235
56	Middle Triassic (Ladinian, 239.5 Ma)	240
57	Middle Triassic (Anisian, 244.6 Ma)	245
58	Permo-Triassic Boundary (252 Ma)	250
59	Late Permian (Lopingian, 256 Ma)	255
60	late Middle Permian (Capitanian, 262.5 Ma)	260
61	Middle Permian (Wordian/Capitanian Boundary 265.1 Ma)	265
62	Middle Permian (Roadian&Wordian, 268.7 Ma)	270
63	Early Permian (late Kungurian, 275 Ma)	275
64	Early Permian (early Kungurian, 280 Ma)	280
65	Early Permian (Artinskian, 286.8 Ma)	285
66	Early Permian (Sakmarian, 292.6 Ma)	290
67	Early Permian (Asselian, 297 Ma)	295
68	Late Pennsylvanian (Gzhelian, 301.3 Ma)	300
69	Late Pennsylvanian (Kasimovian, 305.4 Ma)	305
70	Middle Pennsylvanian (Moscovian, 311.1 Ma)	310
71	Early/Middle Carboniferous (Baskirian/Moscovian boundary, 314.6 Ma)	315
72	Early Pennsylvanian (Bashkirian, 319.2 Ma)	320
73	Late Mississippian (Serpukhovian, 327 Ma)	325
74	Late Mississippian (Visean/Serpukhovian boundary, 330.9 Ma)	330
75	Middle Mississippian (late Visean, 333 Ma)	335
76	Middle Mississippian (middle Visean, 338.8Ma)	340
77	Middle Mississippian (early Visean, 344 Ma)	345
78	Early Mississippian (late Tournaisian, 349 Ma)	350
79	Early Mississippian (early Tournaisian, 354Ma)	355
80	Devono-Carboniferous Boundary (358.9 Ma)	360
81	Late Devonian (middle Famennian, 365.6 Ma)	365

82	Late Devonian (early Famennian, 370 Ma)	370
83	Late Devonian (late Frasnian, 375 Ma)	375
84	Late Devonian (early Frasnian, 380 Ma)	380
85	Middle Devonian (Givetian, 385.2 Ma)	385
86	Middle Devonian (Eifelian, 390.5 Ma)	390
87	Early Devonian (late Emsian, 395 Ma)	395
88	Early Devonian (middle Emsian, 400 Ma)	400
89	Early Devonian (early Emsian, 405 Ma)	405
90	Early Devonian (Pragian, 409.2 Ma)	410
91	Early Devonian (Lochkovian, 415 Ma)	415
92	Late Silurian (Pridoli, 421.1 Ma)	420
93	Late Silurian (Ludlow, 425.2 Ma)	425
94	Middle Silurian (Wenlock, 430.4 Ma)	430
95	Early Silurian (late Llandovery, 436 Ma)	435
96	Early Silurian (early Llandovery, 441.2 Ma)	440
97	Late Ordovician (Hirnantian, 444.5 Ma)	445
98	Late Ordovician (Katian, 449.1 Ma)	450
99	Late Ordovician (Sandbian, 455.7 Ma)	455
100	Middle Ordovician (late Darwillian, 460 Ma)	460
101	Middle Ordovician (early Darwillian, 465 Ma)	465
102	Early Ordovician (Floian/Dapingian boundary, 470 Ma)	470
103	Early Ordovician (late Early Floian, 475 Ma)	475
104	Early Ordovician (Tremadoc, 481.6 Ma)	480
105	Cambro-Ordovician Boundary (485.4 Ma)	485
106	Late Cambrian (Jiangshanian, 491.8 Ma)	490
107	Late Cambrian (Pabian, 495.5 Ma)	495
108	late Middle Cambrian (Guzhangian, 498.8 Ma)	500
109	late Middle Cambrian (early Epoch 3, 505 Ma)	505

110	early Middle Cambrian (late Epoch 2, 510 Ma)	510
111	early Middle Cambrian (middle Epoch 2, 515 Ma)	515
112	Early/Middle Cambrian boundary (520 Ma)	520
113	Early Cambrian (late Terreneuvian, 525 Ma)	525
114	Early Cambrian (middle Terreneuvian, 530 Ma)	530
115	Early Cambrian (early Terreneuvian, 535 Ma)	535
116	Cambrian/Precambrian boundary (541 Ma)	540

1035 \* *Simulations were not run for the time intervals highlighted in italics.*

1036

1037